J. Fluid Mech. (2008), *vol.* 603, *pp.* 431–462. © 2008 Cambridge University Press
doi:10.1017/S0022112008001225 Printed in the United Kingdom

Modelling film flows down a fibre

C. RUYER-QUIL[1], P. TREVELEYAN[2],
F. GIORGIUTTI-DAUPHINÉ[1], C. DUPRAT[1]
AND S. KALLIADASIS[2]

[1]Laboratoire FAST – UMR CNRS 7608, Campus universitaire, 91405 Orsay, France
[2]Department of Chemical Engineering, Imperial College London, London SW7 2AZ, UK

(Received 9 October 2007 and in revised form 21 February 2008)

Consider the gravity-driven flow of a thin liquid film down a vertical fibre. A model of two coupled evolution equations for the local film thickness h and the local flow rate q is formulated within the framework of the long-wave and boundary-layer approximations. The model accounts for inertia and streamwise viscous diffusion. Evolution equations obtained by previous authors are recovered in the appropriate limit. Comparisons to experimental results show good agreement in both linear and nonlinear regimes. Viscous diffusion effects are found to have a stabilizing dispersive effect on the linear waves. Time-dependent computations of the spatial evolution of the film reveal a strong influence of streamwise viscous diffusion on the dynamics of the flow and the wave selection process.

1. Introduction

A liquid film flowing down a vertical fibre is an unstable open-flow hydrodynamic system that exhibits a rich variety of wave phenomena and transitions, ranging from the classical spatio-temporal disorder prompted by the Kapitza instability mode of films falling down vertical planes – hereinafter referred to as ‘K mode’– and characterized by the presence of continuously interacting solitary waves, to the emergence of very regular drop-like wave patterns resulting from the Rayleigh–Plateau instability mode of a liquid layer coating a cylinder – hereinafter referred to as ‘RP mode’ (Kliakhandler, Davis & Bankoff 2001; Duprat *et al.* 2007).

The experimental investigation of flows down fibres was initiated by the studies of Quéré in the context of drawing of wires from liquid baths (Quéré 1990, 1999). Quéré observed the formation of axisymmetric drops, and showed that this break-up process may be arrested by mean flow. Kliakhandler *et al.* (2001) examined experimentally the dynamics of a film flowing down a fibre and reported several wavy regimes, consisting of isolated large-amplitude drops moving at constant speed and shape on a nearly flat substrate, regular periodic wavetrains or interaction events between large drops with smaller ones on the residual film separating the large drops.

The arrest by the mean flow of the drop formation process observed by Quéré was analysed in detail by Kalliadasis & Chang (1994). They computed the solutions to a lubrication-type evolution equation for the film thickness h derived by Frenkel (1992) assuming it to be much smaller than the radius R of the fibre and neglecting inertia. They observed a catastrophic growth of the speed and amplitude of the solitary-wave solutions that closely corresponds to the onset of drops in Quéré’s experiments.

Roy, Roberts & Simpson (2002) extended Frenkel’s equation by including higher-order terms in the small aspect ratio h/R (e.g. in Frenkel’s equation only the leading contribution of the azimuthal curvature to the capillary pressure is retained). Kliakhandler *et al.* (2001) examined the case of film thicknesses of the order of the fibre radii corresponding to their experiments. Their derivation is based on the lubrication approximation but contains an *ad-hoc* step within the framework of this approximation, namely the retention of the full curvature term. Craster & Matar (2006) derived a film-thickness evolution equation very similar to that obtained by Kliakhandler *et al.* (2001) based on the assumption that the total radius of the fluid ring $R + h$ is small compared to the capillary length. However, unlike the Kliakhandler *et al.* (2001) equation, the Craster–Matar equation retains the lower-order approximation of the curvature and is consistent at its level of truncation. Moreover, the time-dependent computations of the Craster–Matar equation show reasonable agreement to the experiments performed by these authors as well as to the study by Kliakhandler *et al.*

All modelling attempts described above assumed negligible inertia effects. Therefore they cannot account for the K hydrodynamic instability mechanism. A decisive first step towards accounting for inertia effects for moderate Reynolds numbers was undertaken by Trifonov (1992) who applied the Kàrmàn–Polhausen averaging technique for a film falling down a planar substrate, introduced first by Shkadov (1967), to formulate a system of two evolution equations for the film thickness h and the flow rate q. Trifonov demonstrated the presence of at least two families of travelling-wave solutions leading to ‘negative’ or ‘positive’ solitary waves in the limit of small wavenumbers. Sisoev *et al.* (2006) carried out transient numerical simulations of Trifonov’s model with periodic forcing at the inlet. The spatial evolution of the waves is then characterized by the selection of the fastest travelling wave having the same frequency with the forcing at the inlet. However, the Kármán–Pohlhausen averaging technique is known to lead to an erroneous estimate of the instability threshold for a film falling down a planar inclined substrate, a direct consequence of neglecting the contribution of the streamwise viscous dissipation (Ruyer-Quil & Manneville 2000). More recently, Roberts & Li (2006) obtained a two-equation model based on a centre-manifold approach by taking into account both inertia and streamwise viscous diffusion, but assumed a small aspect ratio h/R, whereas the reported experimental conditions correspond to $h/R \sim 1$ (Kliakhandler *et al.* 2001; Duprat *et al.* 2007).

In this study we develop a generic modelling approach based on first principles to formulate a two-equation model for the film thickness h and flow rate q. The model overcomes the limitations of the Trifonov and the Roberts & Li models, i.e. it accounts for inertia, streamwise viscous diffusion, both small and $O(1)$ aspect ratios h/R as well as small and large surface tension fluids and is consistent with the above cited lubrication equations in the appropriate limit. In addition, we investigate the role of viscous streamwise effects in the experimental conditions of the Kliakhandler *et al.* and Duprat *et al.* studies and we demonstrate good agreement with these experiments. We also clearly demarcate regions in the parameter space where previous models are valid.

The different tests used for the validation of our model are as follows. (i) The linear stability characteristics of the base flow and their comparison with an Orr–Sommerfeld analysis of the full Navier–Stokes equations and wall and free-surface boundary conditions. A related test here is the analysis of the response of the base flow to a localized perturbation and the ability of the model to capture the absolute/convective instability transition as predicted by Orr–Sommerfeld. (ii) Direct comparisons with experiments of different features of the flow such as travelling-wave characteristics (speed, maximum amplitude).

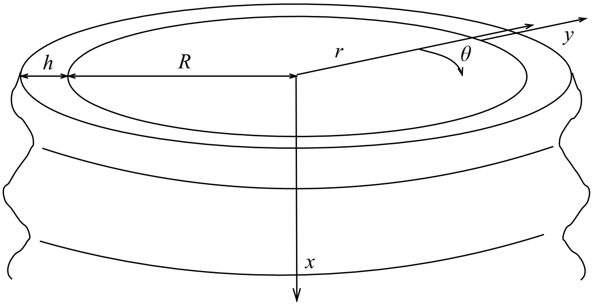

FIGURE 1. Sketch of the profile geometry for a thin liquid film falling down a vertical fibre. A cylindrical coordinate system (r, θ) is chosen at the fibre centreline $r=0$. R is the fibre radius and h is the local film thickness. (x, y) is a Cartesian coordinate system with x the axial/streamwise coordinate along the fibre centreline and $y=r-R$ an outward pointing coordinate normal to the fibre surface and such that $y=0$ corresponds to the fibre surface and $y=h$ to the film surface.

The paper is organized as follows. The governing equations for a film flowing down a vertical fibre and their non-dimensionalization are given in § 2. The boundary-layer approximation is outlined in § 3. A two-equation model is next formulated using a weighted residuals procedure in § 4 which is validated and compared to available experimental data in the linear and nonlinear regimes in § 5 and § 6, respectively. Time-dependent simulations of the spatial evolution of the flow along the fibre are presented in § 7 followed by concluding remarks in § 8.

2. Governing equations

Consider a film falling down a vertical fibre as illustrated in figure 1. The fluid properties, namely viscosity μ, density ρ and surface tension σ, are all assumed to remain constant. Our non-dimensionalization is based on the viscous–gravity time and space scales, $t_\nu = \nu^{1/3} g^{-2/3}$, $l_\nu = \nu^{2/3} g^{-1/3}$, built from the kinematic viscosity $\nu = \mu/\rho$ and the acceleration due to gravity g. Assuming axisymmetric flows without any variation in the azimuthal θ-direction, the equations of motion are:

$$\partial_t u_x + u_x \partial_x u_x + u_r \partial_r u_x = -\partial_x p + 1 + \left[\partial_{rr} + \frac{1}{r}\partial_r + \partial_{xx}\right] u_x, \qquad (2.1a)$$

$$\partial_t u_r + u_x \partial_x u_r + u_r \partial_r u_r = -\partial_r p + \left[\partial_{rr} + \frac{1}{r}\partial_r + \partial_{xx}\right] u_r - \frac{1}{r^2} u_r, \qquad (2.1b)$$

$$\partial_r u_r + \frac{u_r}{r} + \partial_x u_x = 0\,. \qquad (2.1c)$$

They are subject to the no-slip/no-penetration boundary condition at the wall

$$u_r = u_x = 0 \quad \text{at} \quad r = R, \qquad (2.1d)$$

the normal and tangential stress balances at the free surface, $r = R + h(x, t)$

$$\begin{aligned} p = {} & \frac{2}{1+(\partial_x h)^2}\left[-\partial_x h(\partial_r u_x + \partial_x u_r) + \partial_x u_x (\partial_x h)^2 + \partial_r u_r\right] \qquad (2.1e) \\ & -\frac{\Gamma}{[1+(\partial_x h)^2]^{3/2}}\left[\partial_{xx} h - \frac{1}{R+h}(1+(\partial_x h)^2)\right], \end{aligned}$$

$$0 = (1-(\partial_x h)^2)(\partial_r u_x + \partial_x u_r) + 2\partial_x h(\partial_r u_r - \partial_x u_x), \qquad (2.1f)$$

where without loss of generality the pressure of the ambient gas phase has been set equal to zero and the kinematic boundary condition:

$$\partial_t h + u_x \partial_x h - u_r = 0\,. \tag{2.1g}$$

The Kapitza number $\varGamma = \sigma/(\rho \nu^{4/3} g^{1/3}) = (l_c/l_\nu)^2$ compares the surface stress σ/l_ν to the viscous stress μ/t_ν, or equivalently the capillary length $l_c = \sqrt{\sigma/(\rho g)}$ to l_ν. By integrating the continuity equation (2.1*c*) across the film and using the no-slip condition (2.1*d*), the kinematic condition (2.1*g*) can be written as a mass conservation equation,

$$(1 + \alpha h)\partial_t h + \partial_x q = 0, \tag{2.2}$$

where $q \equiv R^{-1} \int_R^{R+h} u_x r \,\mathrm{d}r$ is the flow rate per unit circumference length and $\alpha \equiv 1/R$ is the dimensionless curvature of the cylinder.

Therefore the flow is characterized by the dimensionless Nusselt uniform film thickness h_N, the dimensionless radius R and the Kapitza number $\varGamma$, or equivalently the Reynolds number $Re = q_\mathrm{N}$ which appears implicitly through h_N with q_N the dimensionless flow rate of the Nusselt uniform film solution (q_N and Re will be defined in §4), the dimensionless fibre curvature α and the Weber number $We = \varGamma/h_\mathrm{N}^2 = \sigma/(\rho g \bar{h}_\mathrm{N}^2) = (l_c/\bar{h}_\mathrm{N})^2$ where $\bar{h}_\mathrm{N}$ is the dimensional Nusselt uniform film thickness (hereinafter bars are introduced to distinguish dimensional from dimensionless quantities when necessary).

Note that the classical planar case can be recovered when $\alpha = 0$. This can easily be seen by performing the change of variables $(x, r) \rightarrow (x, y)$ and thus measuring the cross-stream variation from the wall, and by defining $(u, v) \equiv (u_x, u_r)$, corresponding to the usual notations for the streamwise/cross-stream velocity components in the planar case. The dimensionless fibre curvature α then appears in the equations of motion (2.1*a*–*c*) and the normal stress balance (2.1*e*). The transformed equations simplify the comparison between the annular geometry and the planar one: the effect of the annular geometry appears through the terms containing the fibre curvature α and it is easy to verify that setting $\alpha = 0$ gives the governing equations for the planar case.

3. Boundary-layer equations for thin-film flow down a fibre

3.1. *Orders of magnitude assignments*

Assuming slow space and time modulations of the flow allows us to define a formal parameter $\epsilon \sim \partial_{x,t} \ll 1$ and to perform a 'gradient expansion' of the governing equations (2.1*a*–2.1*g*) in ϵ. The smallness of ϵ implies a separation of scales between x and r which in turn dictates a different treatment of the streamwise and cross-stream momentum equations as in boundary-layer theory in aerodynamics. Further we assume that $\alpha h \sim \alpha h_\mathrm{N}$ is at most $O(1)$ or h_N is at most $O(R)$ (in the experiments by Kliakhandler *et al.* (2001) and Duprat *et al.* (2007), $\alpha h_\mathrm{N} = O(1)$). We thus exclude the possibility of large αh_N, in which case the film does not really 'see' the fibre and resembles more a vertical falling free jet (and it is quite likely that the flow will be non-axisymmetric in this case).

The formulation of the boundary-layer equations starts by determining the order of magnitude of the inertia terms in the left-hand side of the cross-stream momentum equation (2.1*b*). Since $\bar{h} \sim \bar{h}_\mathrm{N}$, $u_x \sim \bar{u}_\mathrm{N}/(l_\nu/t_\nu)$ with $\bar{u}_\mathrm{N}$ the dimensional Nusselt uniform film velocity whose scaling can be easily obtained by balancing viscous diffusion in the r-direction with gravity, $\bar{u}_\mathrm{N} \sim g\bar{h}_\mathrm{N}^2/\nu$. We then have $u_x \sim h_\mathrm{N}^2$. The continuity equation (2.1*c*) now indicates that the radial component of the velocity is formally of $O(\epsilon h_{\mathrm{N}}^2)$. Since $x, y \sim h_{\mathrm{N}}$, from $u_x \sim h_{\mathrm{N}}^2 \sim h_{\mathrm{N}}/t$, $t \sim 1/h_{\mathrm{N}}$ and the inertia terms in the left-hand side of the cross-stream momentum equation (2.1*b*) are of $O(\epsilon^2 h_{\mathrm{N}}^3)$. Neglecting these terms, using the relation obtained by differentiating the continuity equation (2.1*c*) once with respect to r, and dropping the streamwise viscous term $\partial_{xx} u_r = O(\epsilon^2 \epsilon h_{\mathrm{N}}^2 / h_{\mathrm{N}}^2) \equiv O(\epsilon^3)$, yields the simplified cross-stream momentum equation, $\partial_r p = -\partial_{xr} u_x$, which can be integrated once with respect to r to give

$$p = p|_h - \partial_x u_x + \partial_x u_x|_h, \tag{3.1}$$

where terms of $O(\epsilon^3 h_{\mathrm{N}}, \epsilon^2 h_{\mathrm{N}}^4)$ have been neglected. This is indeed the case provided that $\epsilon^{3/2} \ll h_{\mathrm{N}} \ll \epsilon^{-1/4}$ and $\alpha \gg \epsilon^{9/4}$, from a detailed examination of the orders of magnitude of the retained over the neglected terms.

The first term $p|_h$ in the approximation for the pressure in (3.1) must be evaluated from the normal stress balance in (2.1*e*) that gives the pressure drop across the free surface. The contribution of the streamwise curvature $\Gamma \partial_{xx} h$ due to surface tension must be kept in our formulation as it is well known from the planar case that this is the principal physical effect that prevents the waves from breaking. However, this term is formally of $O(\Gamma h_{\mathrm{N}} \epsilon^2 / h_{\mathrm{N}}^2) \equiv \Gamma \epsilon^2 / h_{\mathrm{N}}$ and should be neglected, if for example Γ is at most of $O(1)$ and $h_{\mathrm{N}} = O(1)$, as in this case terms of $O(\epsilon^2)$ and higher are neglected in our approximation for the pressure in (3.1). Unless the streamwise curvature is sufficiently large in certain regions/boundary layers of a free-surface deformation such as the steep front edge of a solitary hump: it contains the highest derivative of h multiplied by ϵ^2 and in these boundary layers this derivative is sufficiently large and cannot be neglected. However, proceeding via inner/outer asymptotic expansions is cumbersome if not impossible. It is more convenient to avoid any boundary layers and to stipulate that the streamwise curvature is important throughout a solitary hump and not just in certain regions.

The contribution of the streamwise curvature in (2.1*a*) is $\Gamma \partial_{xxx} h$ with formal order:

$$\Gamma \partial_{xxx} h \sim \Gamma \frac{h_{\mathrm{N}}}{h_{\mathrm{N}}^3} \epsilon^3 \equiv \frac{\Gamma}{h_{\mathrm{N}}^2} \epsilon^3. \tag{3.2}$$

To proceed further we need to assign a relative order between Γ and ϵ. Two cases of particular interest here are large Γ and $\Gamma = O(1)$. The case of large Γ is representative of liquids with high surface tension and small kinematic viscosity such as water ($\Gamma \sim 3000$ at 25°C) while the second case corresponds to liquids with surface tension smaller than that of water and kinematic viscosity much larger than that of water such as silicone oils.

(i) Γ large, 'the strong surface tension limit'. This is quite frequently the case in inertia-driven films on planar substrates where water is used as the working fluid. A convenient order-of-magnitude assignment is $\Gamma = O(\epsilon^{-2})$. For simplicity let us also assume that $h_{\mathrm{N}} = O(1)$ (a sufficiently large Γ/surface tension is required for 'thick' films in order to prevent the waves from breaking). From (3.2), $\Gamma \partial_{xxx} h$ is formally of $O(\epsilon)$ and must be retained since terms of $O(\epsilon^3)$ and higher are neglected. However, at the steep front edge of a solitary pulse and by analogy with the planar case, the pressure gradient $\Gamma \partial_{xxx} h$ due to surface tension and the gravitational acceleration equal to unity in (2.1*a*) balance. Hence, $\Gamma \partial_{xxx} h$ has its formal order, $O(\epsilon)$, throughout except at the front where it increases to $O(1)$. Let us introduce in this region the transformation $x = \kappa h_{\mathrm{N}} x_S$ due to Shkadov (1977) – we shall return to it in §4. We then have:

$$\Gamma\partial_{xxx}h = \Gamma\partial_{x_S x_S x_S}h\frac{1}{\kappa^3 h_{\mathrm{N}}^3} \sim \frac{\Gamma h_{\mathrm{N}}}{\kappa^3 h_{\mathrm{N}}^3} \equiv \frac{\Gamma}{\kappa^3 h_{\mathrm{N}}^2} \sim 1 \Rightarrow \kappa = \left(\frac{\Gamma}{h_{\mathrm{N}}^2}\right)^{1/3} \equiv We^{1/3}. \tag{3.3}$$

In terms of dimensional variables, (3.3) corresponds to the balance $\rho g \sim \sigma\partial_{\bar{x}\bar{x}\bar{x}}\bar{h}$ or $\rho g \sim \sigma\bar{h}_{\mathrm{N}}/l_S^3$ where l_S is the length scale over which the pressure gradient due to streamwise surface tension and gravitational acceleration balance – it corresponds effectively to the characteristic length of the steep front of a solitary wave. We then have $\bar{h}_{\mathrm{N}}/l_S \sim We^{-1/3} = 1/\kappa \sim \epsilon^{2/3}$ so that l_S is much larger than the film thickness $\bar{h}_{\mathrm{N}}$ and the long-wave assumption is not violated. Equivalently, the long-wave assumption is sustained at the front of a solitary wave if $\partial_x h \ll 1$ there. Indeed,

$$\partial_x h = \partial_{x_S}h\frac{1}{\kappa h_{\mathrm{N}}} \sim \frac{h_{\mathrm{N}}}{\kappa h_{\mathrm{N}}} \equiv \frac{1}{\kappa} \sim \epsilon^{2/3}. \tag{3.4}$$

This estimate also shows that $\partial_x h$ at the front of a solitary wave is much larger than its formal order, $O(h_{\mathrm{N}}\epsilon/h_{\mathrm{N}}) \equiv O(\epsilon)$. However, $\partial_x h$ is never larger than unity at the front consistent with our stipulation that we do not have a singular perturbation problem since $\Gamma\partial_{xxx}h$ is important throughout a solitary wave.

(ii) $\Gamma = O(1)$. It is now clear that the order of magnitude of h_{N} with respect to ϵ is crucial for the validity of the boundary-layer approximation. For example, if $h_{\mathrm{N}} = O(1)$, from, (3.2), $\Gamma\partial_{xxx}h \sim \epsilon^3$ and must be neglected. On the other hand if $h_{\mathrm{N}} \sim \epsilon^{-1/5}$, which satisfies the requirement $h_{\mathrm{N}} \ll \epsilon^{-1/4}$ given earlier, then $\Gamma\partial_{xxx}h \sim \epsilon^{17/5} \ll \epsilon^3 h_{\mathrm{N}}^4 \sim \epsilon^{11/5}$ and the contribution of the streamwise curvature must be neglected. Hence h_{N} must be small ('thin' films do not require large Γ/surface tension to prevent the waves from breaking): in order to maintain $\Gamma\partial_{xxx}h$ in our perturbation expansion, it must be much larger than the neglected terms, i.e. $(\Gamma/h_{\mathrm{N}}^2)\epsilon^3 \gg \epsilon^4 h_{\mathrm{N}}, \epsilon^3 h_{\mathrm{N}}^4$ or $h_{\mathrm{N}} \ll \epsilon^{-1/3}, 1$ which are satisfied simultaneously if $h_{\mathrm{N}} \ll 1$.

Again, $\Gamma\partial_{xxx}h$ has its formal order throughout except at the front of a solitary pulse where it must be increased to $\Gamma\partial_{xxx}h \sim 1$. As in case (i), in order to sustain the long-wave approximation we require $\kappa \gg 1$ which is indeed the case since $\kappa = (\Gamma/h_{\mathrm{N}}^2)^{1/3} \gg 1$ for $h_{\mathrm{N}} \ll 1$ but now κ can be much smaller than that in equation (3.4) for case (i) if a tighter lower bound is imposed on h_{N}, e.g. $h_{\mathrm{N}} \gg \epsilon$ instead of $h_{\mathrm{N}} \gg \epsilon^{3/2}$ we obtained earlier: with $\Gamma = O(1)$ and $h_{\mathrm{N}} \gg \epsilon$, $\kappa \ll \epsilon^{-2/3}$ which then implies that in case (ii) the front of a solitary pulse must have a larger slope than in case (i) (and $\Gamma\partial_{xxx}h$ is formally $\ll \epsilon$, the formal order of this term in case (i)). On the other hand this is always the case when the condition $h_{\mathrm{N}} \sim 1$ in case (i) is relaxed: $\kappa_i^{-1} \sim \epsilon^{2/3}h_{\mathrm{N}}^{2/3}$ and $\kappa_{ii}^{-1} \sim h_{\mathrm{N}}^{2/3}$. Physically, in case (ii) surface tension is not strong enough to prevent the slope from increasing but again the slope $\partial_x h$ is never larger than unity, which is consistent with our stipulation that we do not have a singular perturbation problem. Equivalently, for a given h_{N}, increasing Γ decreases the slope at the front.

3.2. *Boundary-layer approximation for large Γ*

We now return to the evaluation of the term $p|_h$ in the approximation for the pressure in (3.1) in case (i) with $\Gamma = O(\epsilon^{-2})$ and $h_{\mathrm{N}} = O(1)$. In the first instance let us neglect terms of $O(\epsilon^3)$ and higher associated with the viscous part of the pressure in the normal stress balance (2.1*e*). Note that independently of the order of h_{N}, $1/(R+h) \equiv \alpha/(1+\alpha h) = O(\alpha)$: $\alpha/(1+\alpha h) \sim \alpha$ for $\alpha h \ll 1$ and $\sim \alpha$ for $\alpha h = O(1)$. Hence by neglecting terms $O(\epsilon^2, \epsilon^2\alpha) = O(\epsilon^2)$, since in the particular case we are considering $h_{\mathrm{N}} = O(1)$ which with αh_{N} at most of $O(1)$ implies that α is at most of

$O(1)$, the pressure on the free surface is given by:

$$p|_h = -2\partial_x h \partial_r u_x|_h + 2\partial_r u_r|_h - \Gamma \left[\partial_{xx} h - \frac{1}{R+h} \left(1 - \frac{1}{2} (\partial_x h)^2 \right) \right]. \tag{3.5}$$

This expression can be further simplified by considering the tangential stress boundary condition (2.1*f*) where terms of $O(\epsilon^3)$ and higher are neglected:

$$\partial_r u_x|_h = 2\partial_x h \left(\partial_x u_x|_h - \partial_r u_r|_h \right) - \partial_x u_r|_h + (\partial_x h)^2 \partial_r u_x|_h. \tag{3.6}$$

All terms in the right-hand side of this equation are of $O(\epsilon^2)$ and hence the contribution of the term $\partial_x h \partial_r u_x|_h$ in (3.5) is of $O(\epsilon^3)$ and can be neglected so that the pressure field is

$$p = -\partial_x u_x + \partial_x u_x|_h + 2\partial_r u_r|_h - \Gamma \left[\partial_{xx} h + K_{\mathrm{az}} \right], \tag{3.7}$$

where terms of $O(\epsilon^2, \epsilon^2\alpha) = O(\epsilon^2)$ are neglected, which is indeed the case provided that $\epsilon^2 \ll \alpha$ and α at most of $O(1)$ (again from a detailed examination of the orders of magnitude of the retained over the neglected terms), and where

$$K_{\mathrm{az}} = -\frac{1}{R+h} \left(1 - \frac{1}{2} (\partial_x h)^2 \right) \equiv -\frac{\alpha}{1+\alpha h} \left(1 - \frac{1}{2} (\partial_x h)^2 \right) \tag{3.8}$$

is the approximation of the azimuthal curvature of the free surface obtained by neglecting terms of $O(\epsilon^4\alpha) = O(\epsilon^4)$ and higher. Note that with $\alpha \to 0$, $\alpha/(1+\alpha h) \to 0$ and $K_{\mathrm{az}} \to 0$ corresponding to the planar limit. Also, since $h_{\mathrm{N}} = O(1)$, $\alpha \to 0$ is equivalent to $\alpha h \to 0$. In the general case, however, when $\alpha h \to 0$, $\alpha/(1+\alpha h) \to \alpha$ corresponding to a very thin film compared to the fibre radius but we still have the azimuthal curvature effect: $\alpha h \to 0$ does not necessarily imply the planar limit when the condition $h_{\mathrm{N}} = O(1)$ is relaxed – see also our discussion at the end of § 2.

Substituting (3.7) into the streamwise momentum equation (2.1*a*) then leads to the following consistent equation up to $O(\epsilon^2)$,

$$\begin{aligned} \partial_t u_x + u_x \partial_x u_x + u_r \partial_r u_x - \left[\partial_{rr} + \frac{1}{r}\partial_r + 2\partial_{xx} \right] u_x \\ = 1 - \partial_x \left[\partial_x u_x|_h + 2\partial_r u_r|_h \right] + \Gamma \left\{ \partial_{xxx} h + \partial_x K_{\mathrm{az}} \right\}, \end{aligned} \tag{3.9}$$

where terms of $O(\epsilon^3)$ and higher have been neglected.

Case (ii) is treated in Appendix A. By analogy now with the planar case where quite frequently $\Gamma = O(\epsilon^{-2})$ as noted earlier, equation (3.9) where terms of $O(\epsilon^3)$ and higher are neglected will be referred to as the 'second-order boundary-layer equation' for the problem of film flow down a fibre and for simplicity our analysis in § 4 is based on case (i). The set of equations to be solved at $O(\epsilon^2)$ (this refers to the truncation of the ϵ-expansion if for example case (ii) is considered), the 'second-order boundary-layer equations', consists of the streamwise momentum equation in the boundary-layer approximation (3.9), the continuity equation (2.1*c*), the no-slip/no-penetration condition at the wall (2.1*d*), the tangential stress balance at the free surface (3.6) and the mass conservation (2.2) or equivalently (2.1*g*). Notice that, when truncated at $O(\epsilon)$ as in the approach followed by Trifonov (1992) and Sisoev *et al.* (2006), the boundary-layer equations do not account for the streamwise viscous diffusion terms $-\partial_x[\partial_x u_x|_h + 2\partial_r u_r|_h]$ in (3.9) and $2\partial_x h(\partial_x u_x|_h - \partial_r u_r|_h) - \partial_x u_r|_h + (\partial_x h)^2 \partial_r u_x|_h$ at the right-hand side of the tangential stress boundary condition in (3.6).

4. Formulation of a low-dimensional model

We now develop a low-dimensional model with a systematic reduction procedure based on a combination of the long-wave approximation and a projection of the velocity field on an appropriately chosen set of test functions. Our approach is not limited to a small ratio of the film thickness to the fibre radius and does not require precise and overly restrictive stipulations on the order of magnitude for this ratio – recall for example from our analysis in § 2 that in case (i) with $h_{\mathrm{N}} = O(1)$, $\epsilon^2 \ll \alpha$ and α at most of $O(1)$ so that αh_{N} could be small or $O(1)$. As pointed out earlier, for simplicity we present in this section the formulation of the model for case (i). Case (ii) can be treated similarly; the final equations are the same for both cases.

4.1. *First-order model*

Let us first consider the case of the Nusselt uniform layer: assuming no modulations of the free surface, $\partial_x = \partial_t = 0$, the basic/Nusselt flow satisfies

$$\mathscr{L}(u_x) = -1 \qquad \text{with} \qquad u_x|_R = 0, \quad \partial_r u_x|_h = 0, \tag{4.1}$$

where $\mathscr{L}$ denotes the (friction) linear differential operator, $\mathscr{L} \equiv \partial_{rr} + r^{-1}\partial_r$. The solution of (4.1) is simply

$$u_x = \frac{1}{2}(R+h)^2 \ln\left(\frac{r}{R}\right) - \frac{1}{4}(r^2 - R^2) \equiv u_{x,0}, \tag{4.2}$$

which can also be written as

$$u_x = h^2 f_{\alpha h}(\hat{y}), \quad f_{\alpha h}(\hat{y}) \equiv -\frac{1}{4}\hat{y}^2 - \frac{1}{2\alpha h}\hat{y} + \frac{1}{\alpha h}\left[1 + \frac{1}{2}\alpha h + \frac{1}{2\alpha h}\right] \ln(1 + \alpha h\, \hat{y}), \tag{4.3}$$

where $\hat{y} = y/h \equiv (r - R)/h$ is a reduced cross-stream coordinate. Therefore, the effect of the curvature of the cylinder on the velocity profile of the uniform film solution is measured by the local aspect ratio $\alpha h = h/R$. Notice that in the limit $\alpha h \to 0$, which without specifying the order of h_{N} corresponds either to the planar limit or to a very thin film compared to the fibre radius (recall, however, from § 3 that due to the condition $h_{\mathrm{N}} = O(1)$ in case (i), the limits $\alpha \to 0$ and $\alpha h \to 0$ are equivalent), the velocity profile is parabolic,

$$f_0 \equiv \lim_{\alpha h \to 0} f_{\alpha h} = \hat{y} - \frac{1}{2}\hat{y}^2,$$

as expected.

Let us now use for the x-velocity a projection of the form,

$$u_x = a_{0,0}(x,t) g_{0,0}(r; h(x,t)) + \sum_{m=1}^{m_{\max}} \sum_{n=0}^{n_{\max}} a_{m,n}(x,t) g_{m,n}(r) \tag{4.4}$$

while the radial component is obtained by integrating the continuity equation (2.1*c*):

$$u_r = -\frac{1}{r}\int_R^r \partial_x u_x(x,\zeta,t)\zeta\, \mathrm{d}\zeta. \tag{4.5}$$

$g_{0,0} \equiv u_{x,0}$ is precisely the Nusselt velocity profile so that (4.4) simply reduces to $u_{x,0}(r; h(x,t))$ and $a_{0,0} = 1$ if the film remains uniform. Consequently, the test functions $g_{m,n}$ account for the deviations of the velocity field from the Nusselt profile and their amplitudes are at most $O(\epsilon)$ quantities. Concerning the particular choice of test functions, we notice that monomials/powers of r and $\ln(r)$ constitute a closed set of functions with respect to differentiations and products involved in the momentum balance (3.9) and the linear operator $\mathscr{L}$. A plausible choice therefore is $g_{m,n} \equiv [(r-R)^m]\,[\ln(r/R)]^n$ which satisfy the no-slip/no-penetration condition on the wall, (2.1d). Note that it can easily be shown that the above expressions for u_x, u_r are consistent with their order-of-magnitude assignments in § 3 obtained from simple scaling arguments.

After multiplication now of the momentum balance (3.9) by r^2, truncation at $O(\epsilon)$ and substitution of the projection (4.4) for the streamwise component of the velocity u_x, we are led to a polynomial in r and $\ln(r)$, say $\mathscr{P}(r, \ln(r))$, that is uniformly equal to zero. Cancelling all its monomials in r and $\ln(r)$ thus yields a number of independent relations equal to the number of unknowns $a_{m,n}$ if $m_{\max}$ and $n_{\max}$ are chosen sufficiently large. Further, since $a_{m,n}$, $m+n \geqslant 1$ are $O(\epsilon)$ corrections to the Nusselt velocity profile, their derivatives can be neglected at that order, and a linear system is obtained. Inversion of this linear system gives the amplitudes $a_{m,n}$, $m+n \geqslant 1$, as functions of $a_{0,0}$ and h, and an evolution equation for $a_{0,0}$ coupled to the evolution of the film thickness h through the mass conservation equation (2.2). The number of non-zero coefficients $a_{m,n}$, i.e. of amplitudes that are of $O(\epsilon)$, can be estimated from the degrees in r and $\ln(r)$ of the advection terms and by parity arguments. Finally, the corrections to the Nusselt velocity profile induced by the deformations of the film surface can be accounted for at $O(\epsilon)$ with seven test functions $g_{m,n}$.

The actual determination of the amplitudes $a_{m,n}$ requires some cumbersome algebraic manipulations that can be substantially simplified with the use of a weighted residuals approach such as the Galerkin or collocation method. With these methods, appropriate weights $w_{m,n}(r)$ are chosen and residuals $\mathscr{R}_{m,n} = \langle w_{m,n} | \mathscr{P} \rangle$ are evaluated where $\langle \cdot | \cdot \rangle$ is an inner product defined over the depth of the film $R \leqslant r \leqslant R + h(x,t)$. Setting the residuals $\mathscr{R}_{m,n}$ equal to zero, or equivalently projecting the polynomial $\mathscr{P}(r, \ln(r))$ onto zero, thus yields a system to be solved for the amplitudes $a_{m,n}$. If the number of test functions is chosen sufficiently large, the number of residuals is equal to the number of independent relationships obtained by setting $\mathscr{P}(r, \ln(r))$ uniformly to zero, so that equivalent systems of equations are found leading to the same system of evolution equations for h and $a_{0,0}$. We look for the best choice for the scalar product and the weighting functions $w_{m,n}$ that leads to the final result with a minimum of algebra.

The mass conservation equation (2.2) is exact and can be kept in a straightforward manner if the flow rate q is substituted with the amplitude of the Nusselt profile $a_{0,0}$ which can easily be done through the definition $q = R^{-1} \int_R^{R+h} u_x r \, \mathrm{d}r$ given in § 2,

$$a_{0,0} = \frac{q}{R^{-1} \displaystyle\int_R^{R+h} g_{0,0}(r\,;h) r \, \mathrm{d}r} - \sum_{m>1,n>1} a_{m,n} \frac{\displaystyle\int_R^{R+h} g_{m,n}(r) r \, \mathrm{d}r}{\displaystyle\int_R^{R+h} g_{0,0}(r\,;h) r \, \mathrm{d}r} \equiv \frac{3q}{h^3 \phi(\alpha h)} + O(\epsilon), \tag{4.6}$$

where ϕ is a measure of the departure of the flow-rate dependence on the film thickness from the planar case $q \equiv \frac{1}{3} h^3$, $\phi(\alpha) \equiv \int_0^1 f_{\alpha h}(\xi)(1+\alpha\xi) \, \mathrm{d}\xi / \int_0^1 f_0(\xi) \, \mathrm{d}\xi$ (the explicit functional dependence on α can be obtained from (B 1) in Appendix B with $b \to 1+\alpha$). The derivation of (2.2) through integration of the continuity equation (2.1c), suggests the use of the inner product $\langle \cdot | \cdot \rangle = \int_R^{R+h} \cdot \cdot \, r \, \mathrm{d}r$.

Considering next the streamwise momentum balance truncated at first order, the residual corresponding to a given weight function $w(r)$ is

$$\int_R^{R+h} \left(\partial_t u_x + u_x \partial_x u_x + u_r \partial_r u_x - \mathscr{L}(u_x) - 1 - \Gamma \left\{ \partial_{xxx} h + \partial_x K_{\mathrm{az}} \right\} \right) r w(r) \, \mathrm{d}r = 0 . \tag{4.7}$$

Substituting for u_x the projection (4.4) and truncating (4.7) at order ϵ, the fields $a_{m,n}$, $m, n \geqslant 1$, corresponding to the corrections to the uniform-film profile $f_{\alpha h}$, may enter into the calculation only through the evaluation of the zeroth order terms:

$$\int_R^{R+h} [\mathscr{L}(u_x)+1]\, r w(r)\, \mathrm{d}r = [r(w\partial_r u_x - u_x w')]_R^{R+h} + \int_R^{R+h} [u_x\, \mathscr{L}(w) + w]\, r\, \mathrm{d}r. \quad (4.8)$$

The evaluation of these terms can be drastically simplified by demanding that the weight function satisfies

$$\mathscr{L}(w) = A \qquad \text{with} \qquad w(R) = 0, \quad w'(R+h) = 0, \quad (4.9)$$

where A is a constant, so that the integral $\int_R^{R+h} u_x\, \mathscr{L}(w)\, r \mathrm{d}r$ is proportional to the flow rate q. The system (4.9) is similar to (4.1) when $A = -1$, which reflects the fact that the operator $\mathscr{L}$ is self-adjoint with respect to the chosen inner product. Consequently, the choice $w \equiv u_{x,0}$ is the most appropriate, which corresponds precisely to the Galerkin method.

After truncation at $O(\epsilon)$ and use of the mass balance (2.2), which enables the substitution of $-\partial_x q/(1+\alpha h)$ for $\partial_t h$, equation (4.7) becomes:

$$\partial_t q = -F(\alpha h)\frac{q}{h}\partial_x q + G(\alpha h)\frac{q^2}{h^2}\partial_x h + I(\alpha h) \times \left[h - \frac{3}{\phi(\alpha h)}\frac{q}{h^2} + \varGamma h\left\{\partial_{xxx}h + \partial_x K_{\mathrm{az}}(\alpha h, \alpha)\right\}\right]. \quad (4.10)$$

Coefficients F, G and I are positive functions of αh defined in Appendix B, equation (B 1). The Nusselt solution is recovered in the uniform thickness limit, $\partial_t \to 0$, $\partial_x \to 0$, where

$$q = \frac{h^3}{3}\phi(\alpha h). \quad (4.11)$$

Notice the dependence of the azimuthal curvature K_{az} on both the aspect ratio αh and α. Nevertheless, the product $h\partial_x K_{\mathrm{az}}$ depends on αh only, a consequence of the averaging procedure across the film and the elimination of the pressure from the cross-stream component of the momentum equation. Hence, the planar geometry now corresponds to both limits $\alpha \to 0$ and $\alpha h \to 0$, when the condition $h_{\mathrm{N}} = O(1)$ is relaxed (in both cases the azimuthal curvature vanishes), unlike the full Navier–Stokes equations in (2.1).

The integral momentum balance (4.10) is similar to that obtained by Trifonov (1992) by averaging the first-order boundary-layer equation with a uniform weight and assuming a self-similar velocity distribution, $u_x = a_{0,0}u_{x,0}$. The coefficients F, G and I obtained by Trifonov are given in Appendix B, equation (B 2). However, the Trifonov model is not consistent at $O(\epsilon)$ since it does not account for the deviations of the velocity profile from the Nusselt profile $u_{x,0}$.

4.2. *Second-order model*

Although the first-order model (2.2), (4.10) is consistent at $O(\epsilon)$, it does not take into account important physical features such as the dispersion induced by the streamwise second-order viscous dissipative terms. These effects can be taken into account by extending the derivation process to $O(\epsilon^2)$. Starting from the second-order momentum balance (3.9), averaging with the weight $u_{x,0}$ and replacing $-\partial_x q/(1+\alpha h)$ with $\partial_t h$, we obtain

$$\begin{aligned}
\partial_t q = & -F(\alpha h)\,\frac{q}{h}\partial_x q + G(\alpha h)\,\frac{q^2}{h^2}\partial_x h \\
& + I(\alpha h)\left[h - \frac{3}{\phi(\alpha h)}\frac{q}{h^2} + \Gamma h\left\{\partial_{xxx}h + \partial_x K_{\mathrm{az}}(\alpha h, \alpha)\right\}\right] \\
& + J(\alpha h)\frac{q}{h^2}(\partial_x h)^2 - K(\alpha h)\frac{\partial_x q\,\partial_x h}{h} - L(\alpha h)\frac{q}{h}\partial_{xx}h \\
& + M(\alpha h)\partial_{xx}q + \mathscr{K}(h, q, \alpha)\,.
\end{aligned} \tag{4.12}$$

Comparing (4.12) to (4.10) shows that the additional terms taking into account the second-order effects have been collected in the last line row of (4.12). The first four terms in this line arise from the streamwise viscous dissipation, whereas $\mathscr{K}$ contains second-order inertial terms corresponding to the first-order corrections to the Nusselt velocity profile and is a rather complex function of q, h and their derivatives. Although the inclusion of these inertial terms ensures that the system (2.2), (4.12) is consistent at $O(\epsilon^2)$, the nonlinearities involved in $\mathscr{K}$ may drastically restrict the range of parameters for which solutions to (2.2), (4.12) exist and can be favourably compared to experimental data. Indeed, in the planar case, a 'regularization' procedure was necessary to avoid the presence of non-physical blow-ups of the time-dependent solutions due to second-order inertial terms even at moderate Reynolds numbers (Scheid, Ruyer-Quil & Manneville 2006). In fact, in the planar case, dropping the second-order inertial corrections leads to a simplified formulation which satisfactorily captures all physical mechanisms (Ruyer-Quil & Manneville 2000). For these reasons and to reduce the complexity of our second-order model, we neglect hereinafter the second-order inertial effects and set $\mathscr{K} = 0$.

The expressions of the (positive) functions J, K, L and M accounting for the second-order streamwise viscous effects are given in Appendix B, equation (B 3). For $\alpha \ll 1$ (which as pointed out earlier in our average model is equivalent to $\alpha h \ll 1$), (B 1) and (B 3) give at $O(\alpha^2)$:

$$F(\alpha h) \approx \frac{17}{7} - \frac{1873}{1344}\alpha h + \frac{425623}{564480}\alpha^2 h^2 \approx 2.43 - 1.39\,\alpha h + 0.75\,\alpha^2 h^2, \tag{4.13a}$$

$$G(\alpha h) \approx \frac{9}{7} - \frac{9}{448}\alpha h - \frac{27423}{62720}\alpha^2 h^2 \approx 1.29\, - 0.02\,\alpha h - 0.44\,\alpha^2 h^2, \tag{4.13b}$$

$$\frac{3I(\alpha h)}{\phi(\alpha h)} \approx \frac{5}{2} - \frac{25}{24}\alpha h + \frac{1391}{2016}\alpha^2 h^2 \approx 2.5 - 1.04\,\alpha h + 0.69\,\alpha^2 h^2 \tag{4.13c}$$

$$I(\alpha h) \approx \frac{5}{6} + \frac{35}{72}\alpha h + \frac{47}{6048}\alpha^2 h^2 \approx 0.83 + 0.49\,\alpha h + 0.0078\,\alpha^2 h^2, \tag{4.13d}$$

$$J(\alpha h) \approx 4 + \frac{7}{12}\alpha h - \frac{1679}{1008}\alpha^2 h^2 \approx 4 + 0.58\,\alpha h - 1.67\,\alpha^2 h^2, \tag{4.13e}$$

$$K(\alpha h) \approx = \frac{9}{2} + \frac{21}{8}\alpha h - \frac{5641}{1120}\alpha^2 h^2 \approx 4.5 + 2.62\,\alpha h - 5.04\,\alpha^2 h^2, \tag{4.13f}$$

$$L(\alpha h) \approx 6 - \frac{1}{4}\alpha h + \frac{259}{240}\alpha^2 h^2 \approx 6 - 0.25\,\alpha h + 1.08\,\alpha^2 h^2, \tag{4.13g}$$

$$M(\alpha h) \approx \frac{9}{2} - \frac{15}{8}\alpha h + \frac{559}{224}\alpha^2 h^2 \approx 4.5 - 1.87\,\alpha h + 2.50\,\alpha^2 h^2, \tag{4.13h}$$

which can be contrasted with the result obtained by Roberts & Li (2006). These authors also eliminated the cross-stream variable dependence through a ‘centre manifold’ approach that led to a system of two evolution equations for the film thickness h and an averaged axial velocity $\langle u\rangle = q/h$. However, the procedure is cumbersome and was limited to $\alpha h_{\mathrm{N}} = O(\epsilon)$ (unlike the experiments by Kliakhandler *et al.* (2001) and Duprat *et al.* (2007) where $\alpha h_{\mathrm{N}} = O(1)$). Recasting this model (referred to hereinafter as the ‘RL model’) in terms of the film thickness h and flow rate q leads to a set of equations similar to (4.12) with

$$\left.\begin{aligned} &F = 2.504, \quad G = 1.356, \quad 3I/\phi = \pi^2/4 - \alpha h + 0.647\,\alpha^2 h^2 \\ &I = \pi^2/12 + 0.4891\,\alpha h, \quad J = 3.459, \quad K = 3.353, \\ &L = 4.676, \quad M = 4.093. \end{aligned}\right\} \tag{4.14}$$

The coefficients of the expansion (4.13) are close to those of the RL model (4.14) in spite of the differences between the two approaches.

Finally, in the planar limit, $\alpha = 0$, the second-order simplified model derived by Ruyer-Quil & Manneville (2000) is recovered from (4.12) with coefficients given by:

$$F = \tfrac{17}{7}, \quad G = \tfrac{9}{7}, \quad I = \tfrac{5}{6}, \quad 3I/\phi = \tfrac{5}{2}, \quad J = 4, \quad K = \tfrac{9}{2}, \quad L = 6, \quad M = \tfrac{9}{2}. \tag{4.15}$$

4.3. *Shkadov scaling*

Comparisons of the waves appearing on the surface of the film can be greatly simplified by introducing a scaling based on the uniform film thickness h_{N} and the average velocity of the uniform flow $u_{\mathrm{N}} = q_{\mathrm{N}}/h_{\mathrm{N}} = h_{\mathrm{N}}^2\phi(\alpha h_{\mathrm{N}})/3$. However, to avoid the introduction of a numerical coefficient 3, we shall use $3u_{\mathrm{N}} = h_{\mathrm{N}}^2\phi(\alpha h_{\mathrm{N}})$ instead. Our analysis is further simplified with the scaling first introduced by Shkadov for a film falling down a vertical plane (Shkadov 1977) which was used in § 3.1 (with this scaling, the number of parameters reduces to only one in the case of our first-order model as for the Trifonov model (Sisoev *et al.* 2006)): we introduce different length scales for the streamwise and cross-stream direction, κh_{N} (or in terms of dimensional variables $l_S \sim \kappa \bar{h}_{\mathrm{N}}$ introduced in § 3.1) and h_{N}, respectively. The parameter κ was defined in § 3.1.

Using the transformation $\mathscr{T} : [x \mapsto \kappa h_{\mathrm{N}} x, (y, h) \mapsto (h_{\mathrm{N}} y, h_{\mathrm{N}} h), t \mapsto t\kappa/[h_{\mathrm{N}}\phi(\alpha h_{\mathrm{N}})]$, $(u, v) \mapsto (h_{\mathrm{N}}^2\phi(\alpha h_{\mathrm{N}})u, h_{\mathrm{N}}^2\phi(\alpha h_{\mathrm{N}})v/\kappa)$, $q \mapsto (h_{\mathrm{N}}^3\phi(\alpha h_{\mathrm{N}})q]$, the mass conservation equation (2.2) and the averaged momentum balance (4.12) are

$$\partial_t h = -\frac{1}{1+\tilde{\alpha}h}\partial_x q, \tag{4.16a}$$

$$\begin{aligned} \delta\partial_t q = {} & \delta\left[-F(\tilde{\alpha}h)\,\frac{q}{h}\partial_x q + G(\tilde{\alpha}h)\,\frac{q^2}{h^2}\partial_x h\right] + \frac{I(\tilde{\alpha}h)}{\phi(\tilde{\alpha})}\left[-\frac{3\phi(\tilde{\alpha})}{\phi(\tilde{\alpha}h)}\frac{q}{h^2}\right. \\ & \left. +h\left\{1 + \partial_{xxx}h + \frac{\beta}{(1+\tilde{\alpha}h)^2}\partial_x h - \frac{1}{2}\partial_x\left(\frac{\tilde{\alpha}}{1+\tilde{\alpha}h}(\partial_x h)^2\right)\right\}\right] \\ & +\eta\left[J(\tilde{\alpha}h)\frac{q}{h^2}(\partial_x h)^2 - K(\tilde{\alpha}h)\frac{\partial_x q\,\partial_x h}{h} - L(\tilde{\alpha}h)\frac{q}{h}\partial_{xx}h + M(\tilde{\alpha}h)\partial_{xx}q\right], \end{aligned} \tag{4.16b}$$

where the parameter set $(h_{\mathrm{N}}, \mathit{\Gamma}, \alpha)$ has been replaced by $(\delta, \eta, \tilde{\alpha})$ corresponding to a reduced Reynolds number,

$$\delta \equiv \frac{h_{\mathrm{N}}^3\phi(\alpha h_{\mathrm{N}})}{\kappa} = \frac{3Re}{\kappa}, \tag{4.17}$$

a viscous dispersion parameter (this term will be clarified in § 5.3),

$$\eta \equiv 1/\kappa^2 = We^{-2/3} = (\bar{h}_{\mathrm{N}}/l_c)^{4/3}, \tag{4.18}$$

and the aspect ratio,

$$\tilde{\alpha} \equiv \alpha h_{\mathrm{N}} = h_{\mathrm{N}}/R\,. \tag{4.19}$$

The parameter η appears along with streamwise dissipative terms which contribute to the dispersion of the waves as discussed later on.

Besides the introduction of the parameters δ, $\tilde{\alpha}$ and η in equation (4.16*b*), the transformation $\mathscr{T}$ modifies the coefficient I to $I/\phi(\tilde{\alpha})$, which results from our choice of the time scale $h_{\mathrm{N}}^2\phi(\alpha h_{\mathrm{N}})$. Similarly, the expression (4.11) of the flow rate at $O(1)$ becomes

$$q = \frac{h^3}{3}\frac{\phi(\tilde{\alpha} h)}{\phi(\tilde{\alpha})}, \tag{4.20}$$

so that $h = 1$ corresponds to $q = 1/3$ with this scaling. Finally, we have isolated the main contribution from the azimuthal curvature gradient, where the parameter

$$\beta = \tilde{\alpha}^2/\eta = (\bar{h}_{\mathrm{N}}/\bar{R})^{2/3}(l_c/\bar{R})^{4/3} \tag{4.21}$$

defined by Kalliadasis & Chang (1994) appears. This parameter expresses the relative importance of axial and azimuthal curvature effects. Note that the planar geometry is recovered from the rescaled boundary-layer equations (4.16) in the limit $\tilde{\alpha} \to 0$ which also makes $\beta \to 0$ (the azimuthal curvature term vanishes in this limit).

4.4. *Inertialess limit*

For highly viscous fluids or very thin films and since $\tilde{\alpha}$ is at most $O(1)$ (for very thin films $\tilde{\alpha} = O(1)$ implies that the fibre is very thin also) so that $\phi(\tilde{\alpha})$ is at most of $O(1)$, $Re \to 0$ or equivalently $\delta \to 0$. Further, by neglecting the viscous second-order terms, $\eta = 0$, (4.16*b*) gives an expression for q in terms of h which when substituted into (4.16*a*) leads to a single evolution equation for h written in conservative form:

$$\partial_t\left(h + \frac{\tilde{\alpha}}{2}h^2\right) + \partial_x\left[\frac{h^3}{3}\frac{\phi(\tilde{\alpha} h)}{\phi(\tilde{\alpha})}\left(1 + \frac{\beta}{(1+\tilde{\alpha} h)^2}\partial_x h + \partial_{xxx} h\right)\right] = 0\,. \tag{4.22}$$

$h + (\tilde{\alpha}/2)h^2$ corresponds to the volume of fluid contained in a sector of angle $\mathrm{d}\theta$ and axial length $\mathrm{d}x$, that is the ratio of the surface of a planar section to the perimeter of the fibre. Equation (4.22) is very close to the evolution equation derived by Kliakhandler *et al.* (2001) and was studied numerically by Craster & Matar (2006). However, the derivation of Kliakhandler *et al.* (2001) contains an *ad-hoc* step, i.e. the retention of the full curvature term, $[1+(\partial_x h)^2]^{-3/2}[\partial_{xx} h - \{\tilde{\alpha}/[\eta(1+\tilde{\alpha} h)]\}(1+\eta(\partial_x h)^2)]$, instead of its lower-order expression, $\partial_{xx} h - \tilde{\alpha}/[\eta(1+\tilde{\alpha} h)]$. Hereinafter we refer to equation (4.22) as the ‘CM equation’ ((4.22) differs from the Craster–Matar equation only in the choice of scalings) and to (4.22) with the full curvature term as the ‘KDB equation’.

For thick enough fibres, that is $\tilde{\alpha} \to 0$, equation (4.22) reduces to

$$\partial_t h + \partial_x\left[\frac{h^3}{3}\left(1 + \beta\partial_x h + \partial_{xxx} h\right)\right] = 0, \tag{4.23}$$

which is the equation derived initially by Frenkel (1992) and used by Kalliadasis & Chang (1994).

5. Linear stability analysis

5.1. *Dispersion relations*

We now examine the linear stability of the Nusselt flow. We first present the simplest dispersion relations obtained in the inertialess limit and studied by Kliakhandler *et al.* (2001) and Duprat *et al.* (2007).

The normal mode decomposition $h = 1 + \varepsilon h_1 \exp[\mathrm{i}(kx - \omega t)]$, $\varepsilon \ll 1$, of both the KDB equation and CM equation (4.22) where k and ω the wavenumber and wave frequency, respectively, leads to the dispersion relation,

$$\omega = k\, c_k(\tilde{\alpha}) + \frac{\mathrm{i}\,\mathrm{k}^2}{3(1+\tilde{\alpha})}\left(\frac{\beta}{(1+\tilde{\alpha})^2} - k^2\right), \tag{5.1}$$

where c_k is the speed of the linear kinematic wave solutions of (4.22) for small wavenumbers, i.e. in the limit $k \to 0$,

$$c_k = \frac{1}{1+\tilde{\alpha}}\left[1 + \frac{\tilde{\alpha}\phi'(\tilde{\alpha})}{3\phi(\tilde{\alpha})}\right] = \frac{8(b-1)\left(2\log(b)b^2 - b^2 + 1\right)}{3\left(4\log(b)b^4 - 3b^4 + 4b^2 - 1\right)}, \tag{5.2}$$

with $b = 1 + \tilde{\alpha}$.

For $\tilde{\alpha} \ll 1$, in which case the Frenkel evolution equation (4.23) applies, we obtain

$$\omega = k + \frac{\mathrm{i}\,\mathrm{k}^2}{3}\left(\beta - k^2\right). \tag{5.3}$$

Notice that the dispersion relation (5.3) can be recovered from (5.1) through the transformation (Duprat *et al.* 2007)

$$k \to k\,[c_k(1+\tilde{\alpha})]^{1/3}, \quad \omega \to \omega c_k^{4/3}(1+\tilde{\alpha})^{1/3}, \quad \beta \to \beta\, c_k^{2/3}(1+\tilde{\alpha})^{8/3}, \tag{5.4}$$

which leads to the definition of the composite parameter $\beta^\star = \beta\, c_k^{-2/3}(1+\tilde{\alpha})^{-8/3}$.

The parameters β and $\beta^\star$ can be related to the ratio of the characteristic time of advection of a structure over its length and the characteristic time of growth of this structure. Considering the dispersion relation (5.3), the RP instability selects structures whose length closely corresponds to the wavenumber with the maximum temporal growth rate, i.e. $k = \sqrt{\beta/2}$. The ratio of the characteristic time of advection of these structures τ_a to their characteristic time of growth τ_g is

$$\tau_a/\tau_g = \omega_i/\omega_r|_{k=\sqrt{\beta/2}} = \frac{\beta^2}{12}\sqrt{\frac{2}{\beta}} \propto \beta^{3/2}. \tag{5.5}$$

Similarly, in the case of dispersion relation (5.1), the maximum of the temporal growth rate corresponds to $k = \sqrt{\beta}/[\sqrt{2}(1+\tilde{\alpha})]$ and we have

$$\tau_a/\tau_g = \omega_i/\omega_r|_{k=\sqrt{\beta}/[\sqrt{2}(1+\tilde{\alpha})]} = \frac{\beta^2}{12(1+\tilde{\alpha})^5}\frac{\sqrt{2}(1+\tilde{\alpha})}{c_k\sqrt{\beta}} \propto (\beta^\star)^{3/2}, \tag{5.6}$$

and therefore β and $\beta^\star$ compare the advection process at the speed of the kinematic waves to the growth of the RP instability.

The dispersion relations (5.1) and (5.3) cannot account for the K-instability mechanism prompted by inertia. Turning back to the two-equation model (4.16), close to the Nusselt solution we set $h = 1 + \tilde{h}$ and $q = 1/3 + \tilde{q}$ where $\tilde{h} \ll 1$ and $\tilde{q} \ll 1$ and we obtain a single equation for $\tilde{h}$ after elimination of $\tilde{q}$ that we purposely split into two parts by separating odd and even derivatives,

$$3(1+\tilde{\alpha})\frac{I}{\phi}\left[\partial_t + c_k\partial_x\right]\tilde{h} - \eta\left[\frac{L}{3}\partial_{xxx} + (1+\tilde{\alpha})M\partial_{txx}\right]\tilde{h} = \lambda, \qquad (5.7a)$$

$$\left\{\delta(1+\tilde{\alpha})\left[\partial_{tt} + \frac{F}{3}\partial_{tx}\right] + \left[\delta\frac{G}{9} + \frac{\beta}{(1+\tilde{\alpha})^2}\frac{I}{\phi}\right]\partial_{xx}\right\}\tilde{h} + \frac{I}{\phi}\partial_{xxxx}\tilde{h} = -\lambda, \qquad (5.7b)$$

where the coefficients F, G, I, L, M and ϕ are evaluated at $\tilde{\alpha}$. The symbol c_k again denotes the speed (5.2) of the kinematic waves in the limit $k \to 0$. The normal mode decomposition $\tilde{h} = h_1 \exp[\mathrm{i}[k x - \omega t]$ in (5.7), leads to the dispersion relation:

$$D(k,\omega) \equiv \mathrm{i}\left\{3(1+\tilde{\alpha})\frac{I}{\phi}\left[c_k k - \omega\right] + \eta k^2\left[k\frac{L}{3} - \omega(1+\tilde{\alpha})M\right]\right\}$$
$$+\delta(1+\tilde{\alpha})\left[-\omega^2 + \frac{F}{3}\omega k\right] - k^2\left[\delta\frac{G}{9} + \frac{\beta}{(1+\tilde{\alpha})^2}\frac{I}{\phi}\right] + k^4\frac{I}{\phi} = 0. \qquad (5.8)$$

The reason now for splitting (5.7) into two parts becomes clear: the split corresponds to a phase shift of $\pi/2$ in (5.8) between two parts of this equation. The marginal stability of the film is then achieved when the two parts are set to zero independently.

5.2. *Influence of viscous dissipation on the RP-instability*

The instability mechanism of a liquid layer coating a cylinder is similar to the instability of a liquid jet as explained by Rayleigh (1878) in his seminal work. Considering the inertialess limit $\delta \to 0$, (5.8) reduces to the dispersion relation (5.1) of both the KDB and CM evolution equations augmented with the second-order viscous effects $\propto \eta k^2$. Since in the absence of these effects, linear wave solutions to (5.1) travel at the speed c_k of the kinematic waves, the effect of second-order viscous terms can be estimated by substituting kc_k for ω except for the ‘critical term’ $c_k k - \omega$ (Whitham 1974). We obtain

$$\omega = k\,c_k(\tilde{\alpha}) - \eta\Upsilon_\eta(\tilde{\alpha})k^3 + \frac{\mathrm{i}\,k^2}{3(1+\tilde{\alpha})}\left(\frac{\beta}{(1+\tilde{\alpha})^2} - k^2\right), \qquad (5.9)$$

where $\Upsilon_\eta = \phi[(1+\tilde{\alpha})Mc_k - L/3]/[3(1+\tilde{\alpha})I]$ is a positive function of $\tilde{\alpha}$.

The marginal stability of the film is therefore still given by $k_{\mathrm{RP}} = \sqrt{\beta}/(1+\tilde{\alpha})$ which corresponds to the classical result for the RP instability that the neutral dimensional wavelength $2\pi(R + \bar{h}_N)$ is proportional to the maximum diameter of the liquid layer. However, second-order viscous terms have a dispersive effect on the waves by decreasing the speed of the linear waves from c_k to $c_k - \eta\Upsilon_\eta(\tilde{\alpha})k^2$.

5.3. *Mechanism of the K instability mode*

We now consider the limit of non-dominant RP instability mode (β/δ and $\tilde{\alpha}$ sufficiently small). In this case the instability results from the K hydrodynamic mechanism.

First, let us extend to our problem the arguments given by Ooshida (1999) in the framework of Whitham wave-hierarchy theory (Whitham 1974) for the planar geometry, and let us consider small wavenumbers, $k \to 0$, for which both surface tension and second-order viscous effects can be neglected. The linear operator of (5.7*b*) can be thus factorized corresponding to waves propagating at speeds $c_{d\pm}$:

$$c_{d\pm} = \frac{F}{6} \pm \sqrt{\Delta} \qquad \text{with} \qquad \Delta = \frac{F^2}{36} - \frac{1}{9}\frac{G}{1+\tilde{\alpha}} - \frac{\beta}{\delta(1+\tilde{\alpha})^3}\frac{I}{\phi}. \qquad (5.10)$$

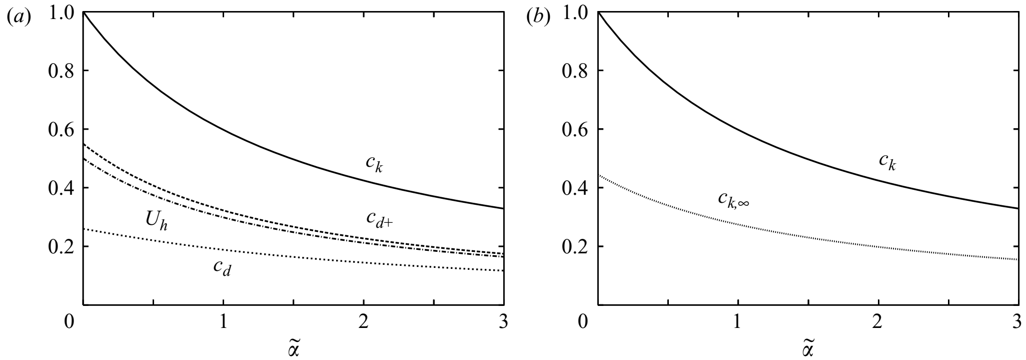

FIGURE 2. (*a*) Speeds c_k of kinematic and $c_{d\pm}$ of dynamic waves as functions of the aspect ratio $\tilde{\alpha} = h_N/R$ in the limit of negligible viscous dispersion and large Reynolds number ($\eta \to 0$ and $\beta/\delta \to 0$). The interfacial velocity $U_h = f_{\tilde{\alpha}}(1)/\phi(\tilde{\alpha})$ of the uniform thickness base flow is also displayed. (*b*) Comparison of the speeds of the kinematic waves in the limit $\eta \to 0$ and $\eta \to \infty$.

In this limit, system (5.7) has a two-wave structure that can be recast into a second-order wave equation,

$$3\frac{I}{\phi}\,[\partial_t + c_k\partial_x]\,\tilde{h} + \delta\,[\partial_t + c_{d-}\partial_x]\,[\partial_t + c_{d+}\partial_x]\,\tilde{h} = 0, \tag{5.11}$$

a situation that corresponds precisely to the wave hierarchy considered by Whitham. The lower-order waves propagating at speed c_k are kinematic waves whose origin is the response to a deformation of the interface to satisfy the kinematic condition (2.1*g*), or equivalently the mass balance (2.2), when the velocity distribution is governed by the balance of the acceleration due to gravity and the wall friction, which in turn leads to the explicit dependence (4.20) of the flow rate q on the film thickness h. Propagating at speed $c_{d\pm}$, the higher-order waves are dynamic waves corresponding to the response of the film to the variation of momentum induced by a deformation of the free surface. Alekseenko, Nakoryakov & Pokusaev (1985) and Ooshida (1999) have similarly derived equations presenting a 'two-wave' structure for the vertical-planar wall geometry. However, these authors did not consider the influence of the streamwise viscous diffusion that is taken into account in (5.7).

Whitham has shown that when a multi-speed equation such as (5.11) holds, an instability occurs whenever the constraint,

$$c_{d-} \leqslant c_k \leqslant c_{d+}, \tag{5.12}$$

is violated, in other words, whenever the speed of the kinematic waves is outside the speed interval allowed to dynamic waves. Figure 2(*a*) compares the speed of the kinematic and dynamics waves given by (5.2) and (5.10) as a function of the aspect ratio $\tilde{\alpha}$ in the limit of dominating inertia ($\beta/\delta \to 0$). Kinematic waves always travel faster than dynamic waves and the stability criterion (5.12) is never satisfied in that case. Small but finite values of β/δ lower the speed of the faster dynamic waves, c_{d+}. Therefore, azimuthal surface-tension effects are destabilizing and the Nusselt constant-thickness solution is always unstable in the limit $k \to 0$. The speeds of kinematic and dynamic waves are compared to the interfacial velocity of the base flow $U_h = f_{\tilde{\alpha}}(1)/\phi(\tilde{\alpha})$ in figure 2(*a*). The fastest dynamic waves travel at a speed which is close to the maximum velocity of the base flow, which indicates that perturbations of the momentum are basically advected by the flow. Consequently, as in the planar case, the K mode of instability results from the ability of the kinematic waves to move much faster than any fluid particle (Smith 1990).

For finite wavenumbers, second-order viscous terms must be accounted for and the speed of kinematic waves is modified into:

$$c_{k,\eta} = \frac{c_k + \eta k^2 \dfrac{\phi}{9(1+\tilde{\alpha})} \dfrac{L}{I}}{1 + \eta k^2 \dfrac{\phi}{3} \dfrac{M}{I}}. \tag{5.13}$$

The dispersive effect of second-order viscous effects on kinematic waves is evident as $c_{k,\eta}$ is a function of ηk^2 (contained in two terms, one in the numerator due to transport of momentum and one in the denominator due to transport of mass). This justifies the term 'viscous dispersion parameter' introduced for η in § 4.3 and we shall also refer to second-order viscous effects as 'viscous dispersion effects'. Considering real wavenumbers, the limit $\eta \to \infty$ gives

$$c_{k,\infty} \equiv \lim_{\eta \to \infty} c_{k,\eta} = \frac{L}{3(1+\tilde{\alpha})M}, \tag{5.14}$$

which is compared to the small-wavenumber limit c_k in figure 2(*b*). Since $c_{k,\infty} < c_{k,\eta} < c_k$, viscous dispersion lowers the speed of the kinematic waves, as observed when the RP mode is dominant (cf. § 5.2), and is therefore stabilizing.

Similarly, axial surface tension modifies the speed of dynamic waves into

$$c_{d\pm ST} = \frac{F}{6} \pm \sqrt{\Delta_{ST}} \qquad \text{with} \qquad \Delta_{ST} = \frac{F^2}{36} - \frac{1}{9}\frac{G}{1+\tilde{\alpha}} + \frac{1}{\delta(1+\tilde{\alpha})}\frac{I}{\phi}\left[k^2 - \frac{\beta}{(1+\tilde{\alpha})^2}\right]. \tag{5.15}$$

Hence, axial surface tension effects accelerate the fastest dynamic waves and tend to stabilise the constant-thickness Nusselt flow.

5.4. *Marginal stability*

Having considered the two limiting cases of dominant RP and K instability modes, let us turn to the marginal stability of the Nusselt flow (ω and k real) as a test of the validity of our modelling approach in comparison with the solutions to the linearized primitive equations. Linearization of the Navier–Stokes equations (2.1) leads to the Orr–Sommerfeld (OS) equation, i.e. a fourth-order ordinary differential equation for the complex streamfunction $\psi(r)$ completed with the linearized stress balances and the no-slip/no-penetration condition at the fibre. The OS equation was solved numerically by using the continuation software AUTO97 (Doedel *et al.* 1997). The starting points for the continuation are the analytical expressions of the solutions in the limit $k \to 0$.

In figure 3, the marginal stability curves corresponding to model (4.16) (upper dashed lines) are compared to those obtained from the Trifonov model (upper thin solid lines) and the OS equation (upper thick solid lines) in the (k_r, δ)-plane. The fluids are Rhodorsil silicon oil v50 ($\rho = 963\,\mathrm{kg\,m^{-3}}$, $\nu = 50 \times 10^{-6}\,\mathrm{m^2\,s^{-1}}$ and $\sigma = 20.8 \times 10^{-3}\,\mathrm{N\,m^{-1}}$; water: $\rho = 998\,\mathrm{kg\,m^{-3}}$, $\nu = 10^{-6}\,\mathrm{m^2\,s^{-1}}$ and $\sigma = 72.5 \times 10^{-3}\,\mathrm{N\,m^{-1}}$), corresponding to Kapitza numbers $\Gamma = 5.48$ and 3376, respectively. Two radii R have been chosen so that they correspond to the same ratio $R/l_c = 0.24$ (for water, $l_c = 2.7$ mm, and for silicon oil v50, $l_c = 1.5$ mm).

As surface tension damps short waves, the regions of stability (labelled 'S') are located above the marginal stability curves. At small values of δ, the RP instability

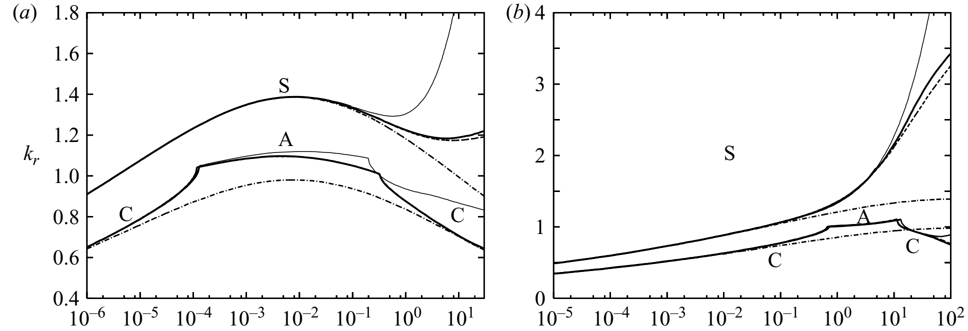

FIGURE 3. Neutral stability curves (upper lines) and loci of the spatially most amplified harmonic perturbations (for convectively unstable flows, C) and of the absolute wavenumber (in the absolutely unstable case, A). The real part of the wavenumber k_r is shown as a function of the reduced Reynolds number δ. Linear stable regions are labelled S. Fluid parameters correspond to (*a*) Rhodorsil silicon oil v50 ($\Gamma = 5.48$) and $R = 0.35$ mm, (*b*) water ($\Gamma = 3376$) and $R = 0.64$ mm. Thick solid and dashed lines refer to OS analysis and to dispersion relation (5.8), respectively (nearly superimposed except for the largest values of δ). Thin solid lines refer to the linear stability analysis of the Trifonov model. The neutral wavenumber k_{RP} and the temporally most amplified wavenumber $k_{\mathrm{RP}}/\sqrt{2}$ of the RP instability (see text) are indicated by dashed-dotted lines.

dominates and all marginal stability curves collapse with $k_r = k_{\mathrm{RP}}$ (dashed-dotted lines). Noticeable differences are observed only at δ above 0.1 for which the hydrodynamic K mode starts to take over. At large values of δ, the marginal curve corresponding to (4.16) remains remarkably close to the OS results, whereas the Trifonov model overestimates the range of unstable wavenumbers. This large discrepancy is mainly a consequence of neglecting the streamwise dissipation terms. As the Kapitza number increases, hence the viscous dispersion parameter η decreases, the marginal stability curve predicted by the Trifonov model is closer to the OS results (compare figures 3*a* and 3*b*). The same trend can be observed with the speed of neutral infinitesimal waves displayed in figure 4(*a*). Neutral wave solutions to the Trifonov model and to (4.16) are kinematic waves travelling at speeds c_k and $c_{k,\eta}$ defined in (5.2) and (5.13), respectively. The agreement of $c_{k,\eta}$ with the speeds of neutral waves solutions of the OS equations is again remarkable.

5.5. *Spatial stability analysis*

Another test of the accuracy of model (4.16) consists of the analysis of the response of the base flow to a localized perturbation. If the resulting wavepacket is advected by the flow, the instability is said to be convective and the flow behaves much like a signal amplifier: at a fixed point in the laboratory frame of reference, the signal eventually dies out if it is not sustained continuously. When the wavepacket is able to move upstream, a self-sustained intrinsic dynamics or ‘global mode’ can be observed and the flow behaves like an ‘oscillator’ (Huerre & Rossi 1998). At a given location, the long-time evolution of the wavepacket is dominated by the part of the signal whose energy remains stationary, hence by the wave corresponding to a zero group velocity, $v_g = \partial\omega/\partial k = 0$, which defines the absolute wavenumber k_0 and frequency ω_0. In the complex k-plane, the condition $v_g = 0$ occurs at a saddle point that must result from the collision of two spatial branches coming from opposite sides of the real axis in order to fulfil the causality condition (Huerre & Rossi 1998).

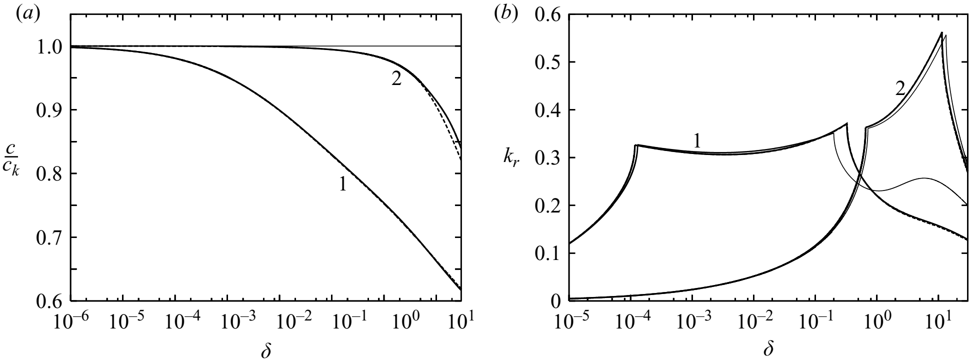

FIGURE 4. (*a*) Wave speed c of linear neutral waves normalized with the speed of the kinematic waves c_k and (*b*) spatial growth rate of the most amplified perturbations (convective case, C) and of the absolute wavenumber (absolutely unstable region, A) as function of δ. Thick solid and dashed lines refer to the OS analysis and to dispersion relation (5.8) whereas thin solid lines are obtained from the Trifonov model. Labels 1 and 2 correspond to Rhodorsil silicon oil v50 ($\Gamma = 5.48$ and $R = 0.35$ mm) and to water ($\Gamma = 3376$ and $R = 0.64$ mm), respectively. See also the caption of figure 3. The increased deviation of the wave speed in (*a*) from unity is a dispersive effect.

The wavenumber k_r of the most spatially amplified perturbation in the convective case and the absolute wavenumber k_{0r} are shown in figure 3(*a*) and are compared to $k_{\text{RP}}/\sqrt{2}$ which corresponds to the most temporally amplified perturbation for dispersion relation (5.1). The corresponding growth rates $-k_i$ and $-k_{0i}$ are shown in figure 4(*b*). In the limit $\delta \rightarrow 0$, all curves converge to $k_r = k_{\text{RP}}/\sqrt{2}$, which is unexpected since the latter corresponds to a temporal stability analysis instead of a spatial one. This limit corresponds to a vanishingly small film thickness, for which both the group velocity v_g and the phase velocity c_k are nearly equal to one and dispersion effects from inertia and viscosity are negligible since $\eta \propto \Gamma h_{\text{N}}^{4/3}$. As $h_{\text{N}} \ll R$, the growth rate is also small and the Gaster transformation, $v_g \approx -\omega_i/k_i$, between temporally and spatially increasing disturbances applies (Gaster 1962). Surprisingly, the wavenumbers k_r of the most amplified spatial perturbations stay close to $k_{\text{RP}}/\sqrt{2}$ even at large values of δ. A remarkable agreement is again observed between results from the model (4.16) and the OS analysis, whereas the Trifonov model, which neglects the stabilizing second-order viscous effects, overestimates the spatial growth rate at large δ for silicon oil.

The RP instability mechanism results from the competition of axial and azimuthal surface-tension effects, irrespective of the presence of a flow. Instead, the K mode results from the competition of dynamic and kinematic waves whose existence is strongly linked to the flow. This explains the fact that the RP mode may trigger an absolute instability (Duprat *et al.* 2007), whereas a film falling down an inclined planar wall can only be convectively unstable (Brevdo *et al.* 1999). The C/A transition from a convective to an absolute instability corresponds to a real absolute frequency. In the inertialess limit, the C/A transition occurs at $\beta = \beta_{ca} \approx 1.507$ for the dispersion relation (5.3) to the Frenkel equation (4.23). Based on the transformation (5.4) from dispersion relation (5.1) to (5.3), we can infer that the C/A transition predicted by the CM equation (4.22) occurs at $\beta^{\star} = \beta_{ca}$. At a given value of R/l_c, $\beta^{\star}$ which compares axial and azimuthal curvatures to the advection by the kinematic waves, reaches a maximum at $\tilde{\alpha} \approx 0.44$ and tends to zero as $\tilde{\alpha} \rightarrow \infty$. Figure 5(*a*) shows the contour line

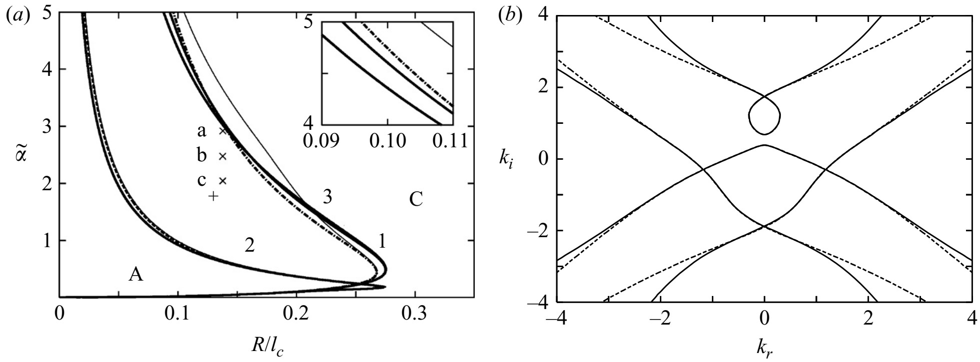

FIGURE 5. (*a*) Absolute A and convective C instability regions in the ($\tilde{\alpha}$, $\bar{R}/l_c$) parameter plane for silicon oil v50 ($\Gamma = 5.48$, labelled 1), water ($\Gamma = 3376$, labelled 2) and castor oil ($\Gamma = 0.45$, labelled 3). The dashed-dotted line corresponds to the C/A boundary $\beta^{\star} = \beta_{ca} \approx 1.507$ for the CM equation (4.22). It is not affected by changing the fluid properties and hence it is the same for the three fluids. The inset is an enlargement of the upper end of the curves. (*b*) Spatial branches in the complex k-plane for silicon oil v50, $q_{\mathrm{N}} = 0.01$ g s^{-1}, $\bar{R} = 0.2$ mm and $\omega_{0i} = 0.126$ (indicated by a + in (*a*): $\delta = 0.1874$, $\tilde{\alpha} = 1.72$, $\eta = 0.143$). Thick solid, thick dashed and thin solid lines refer to the OS analysis, to the dispersion relation (5.8) and to the dispersion relation of the Trifonov model respectively. Values of $\tilde{\alpha}$ and $\bar{R}/l_c$ corresponding to the experiments by Kliakhandler *et al.* (2001) are indicated by crosses. All three experiments and the example shown in (*b*) and indicated by a + in (*a*) are absolutely unstable flows.

$\beta^{\star} = \beta_{ca}$ in the $(R/l_c, \tilde{\alpha})$-plane along with the C/A transition loci obtained from OS and the dispersion relation (5.8). For $R > 0.28 l_c$, the instability is always convective, whereas for $R < 0.28 l_c$, there is an intermediate range of aspect ratios $\tilde{\alpha}$, or film thicknesses, for which an absolute instability can be observed. As we pointed out in § 4, for our low-dimensional models the limit of very small thicknesses $h_{\mathrm{N}} \ll R$ corresponds to the planar case (the same is not true for full Navier–Stokes, however, the linear stability characteristics for $h_{\mathrm{N}} \ll R$ obtained from OS are the same to those of the planar limit) for which it is well known that the instability is always convective, and the RP instability is weakened at large thicknesses $h_{\mathrm{N}} \gg R$ by the decrease of the total curvature $(R + h_{\mathrm{N}})^{-1}$. C/A boundaries predicted by the dispersion relation (5.8) nearly coincide with the OS results, discrepancies being noticeable only for water and for large thicknesses ($\tilde{\alpha} \gg 1$).

For less viscous fluids and higher Kapitza numbers, for example water ($\Gamma = 3376$), the C/A boundaries are shifted significantly downwards, a direct consequence of the higher influence of the hydrodynamic K mode since large values of the aspect ratio $\tilde{\alpha}$ correspond also to large values of the reduced Reynolds number δ. However, the C/A boundary $\beta^{\star} = \beta_{ca}$ given by the CM equation remains unchanged as this equation does not account for the hydrodynamic K mode and hence it is the same when the working fluid changes, for example from a highly viscous liquid, such as silicone oil, to a relatively inviscid liquid, such as water. The influence of the K mode on the absolute instability can also be noted in figure 3(*b*) where the wavenumber k_r corresponding to the maximum growth rate $-k_i$ of spatially amplified perturbations (real ω) in the convective case and to k_{0r} in the absolute case are depicted. The Nusselt flow is absolutely unstable for relatively high values of δ for which a significant discrepancy between the OS marginal curve and the inertialess limit $k = k_{\mathrm{RP}}$ is observed, thus indicating the influence of the K mode.

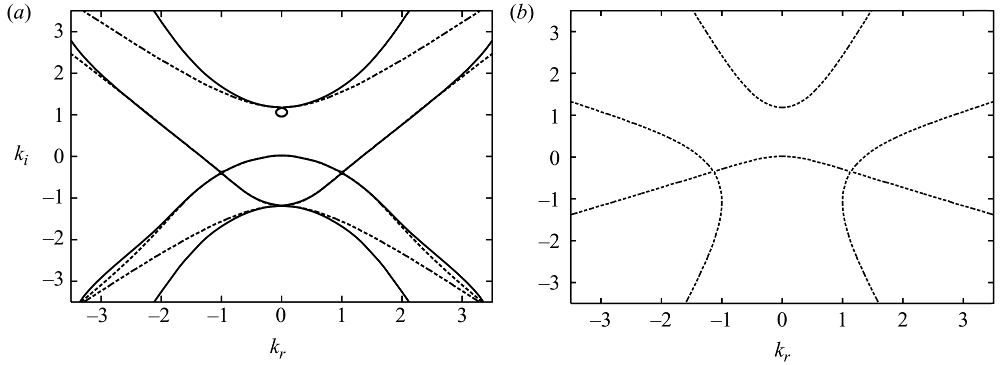

FIGURE 6. Spatial branches in the complex k-plane for castor oil $q_N = 0.021$ g s^{-1}, $\bar{R} = 0.25$ mm and $\omega_i = 0.006$ ($\delta = 0.052$, $\tilde{\alpha} = 2.91$ and $\eta = 0.30$). (*a*) Model (2.2), (4.12); (*b*) CM equation (4.22). Solid lines refer to the OS analysis. Dashed lines in (*a*) and (*b*) refer to the dispersion relations (5.8) and (5.1), respectively.

Let us now focus on the details of the branches of solutions in the complex k-plane. Figure 5(*b*) shows an example of pinching of branches of solutions for the model dispersion relation (5.8) compared to the OS result for a moderately viscous fluid. Chosen parameters correspond to a flow of silicon oil v50 ($\Gamma = 5.48$) on a fibre of radius $R = 0.2$ mm. At small values of $|k|$ the curves are practically indistinguishable. Solutions to (5.8) start to deviate from OS as $|k|$ increases. This remarkable agreement can be understood by considering the derivation of the momentum balance (4.12). Since the neglected second-order inertial corrections $\mathscr{K}(h, q, \alpha)$ are all nonlinear terms, the corresponding dispersion relation (5.8) is exact up to $O(|k|^2)$. For highly viscous fluids and small Kapitza numbers, such as the castor oil used by Kliakhandler *et al.* (2001) ($\nu = 440 \times 10^{-6}$ m^2 s^{-1}, $\rho = 961$ kg m^{-3} and $\sigma = 31 \times 10^{-3}$ N m^{-1} hence $\Gamma = 0.45$), an excellent agreement between the results of the OS analysis and the dispersion relation (5.8) is again achieved (see figure 6(*a*) where an example of pinching of k-branches is given). This could have been expected since in that case the inertialess limit $\delta \to 0$ is perfectly admissible. However, the spatial branches of solutions to the dispersion relation (5.1) corresponding to the CM evolution equation (4.22) show large discrepancies with the results to the OS analysis (compare figure 6*b* to figure 6*a*). These topological differences must be attributed to the second-order viscous dispersion terms that are also neglected in the derivation of the CM equation ($\eta \to 0$).

6. Travelling waves

The experimental response of the flow to a periodic inlet perturbation remains periodic in time at each location in space. Consequently, the integration in time of the mass balance (2.2) gives $\partial_x \langle q \rangle = 0$ where the brackets denote averaging over a temporal period. $\langle q \rangle$ is thus conserved all along the fibre and is equal to its value at the inlet which gives the condition $\langle q \rangle = 1/3$. Travelling waves (TW) of (4.16) are computed with the continuation software AUTO97 (Doedel *et al.* 1997) enforcing the above integral condition on the flow rate at each step of the continuation. The bifurcation diagrams of TW solutions to the two-equation model (4.16) and to the CM equation (4.22) are compared in figure 7(*a*). The parameters in the figure correspond to 'regime b' reported by Kliakhandler *et al.* (see table 1). Figure 7(*b*)

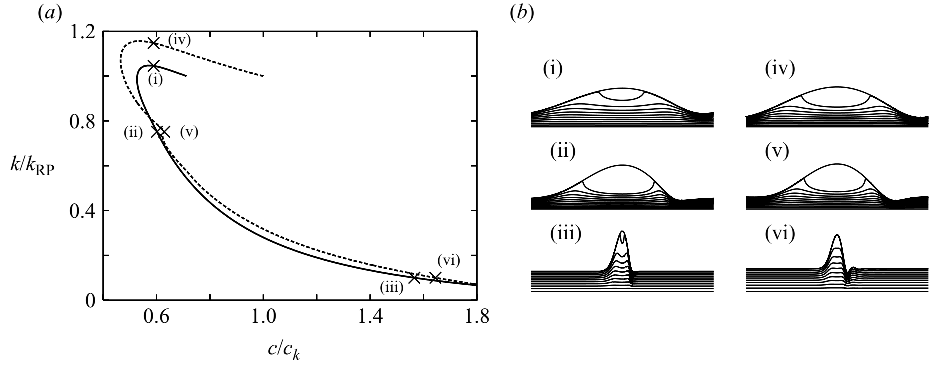

FIGURE 7. (*a*) Speed c of TW solutions as function of their wavenumber k. Parameters correspond to the experimental conditions of Kliakhandler *et al.* (2001) (regime 'b' in table 1, $\delta = 0.024$, $\eta = 0.24$, $\tilde{\alpha} = 2.47$). Solid and dashed lines refer to (4.16) and to the CM equation (4.22), respectively. (*b*) Wave profiles and streamlines in the moving frame for solutions indicated by crosses in (*a*); left: solutions to (4.16); right: solutions to (4.22).

Model	Regime	q_N (mg s^{-1})	h_N (mm)	λ (mm)	c_{expt} (mm s^{-1})	c (mm s^{-1})	h_{max}^{expt} (mm)	h_{max} (mm)	h_{min}^{expt} (mm)	h_{min} (mm)
(4.16)	a	21	0.73	30	25	22.4	1.47	1.34	0.50	0.44
(4.22)						24.7		1.26		0.45
(4.16)	b	11	0.62	6.2	5.4	7.22	1.02	0.92	0.20	0.17
(4.22)						6.98		0.97		0.14
(4.16)	c	5.3	0.51	36	12.0	12.1	1.20	1.09	0.25	0.26
(4.22)						12.6		1.10		0.25

TABLE 1. Comparisons of the characteristics of TW solutions at a given wavelength λ with the experimental values reported by Kliakhandler *et al.* (2001).

shows corresponding wave profiles with regularly spaced streamlines in the moving frame. Only one branch of TW solutions has been found emerging from the marginal linear stability conditions (it does so through a Hopf bifurcation). Since inertia is small here ($\delta = 0.024$) and the RP mode is dominant ($\beta = 25.7$), the TW branch of solutions of (4.16) bifurcates at $k \approx k_{RP}$. However, weakly nonlinear TW solutions of (4.16) travel at a lower speed than the TW solutions of the CM equation (4.22) since the speed of linear kinematic waves is significantly affected by the streamwise viscous terms ($c_{k,\eta} < c_k$). At small wavenumbers, TW accelerate, become more and more localized and terminate in single-humped solitary waves. The speed, amplitude and shape of the solutions (4.16) and (4.22) are comparable in this limit, though our model predicts solitary waves of larger amplitude and speed than the CM equation.

The characteristics of the TW solutions of model (4.16) are compared to the solutions to the CM equation in table 1 for the three regimes reported by Kliakhandler *et al.* (2001). At high flow rate, corresponding to 'regime a' reported by these authors, they observed long and isolated waves moving rapidly and irregularly on a relatively thick substrate. At lower flow rate (termed 'regime b' by these authors), the wave pattern is highly organised with drops of smaller size moving at constant speed and periodicity. At even lower flow rate ('regime c'), the regularity of the wave pattern is again lost with larger waves separated by long and irregular substrates.

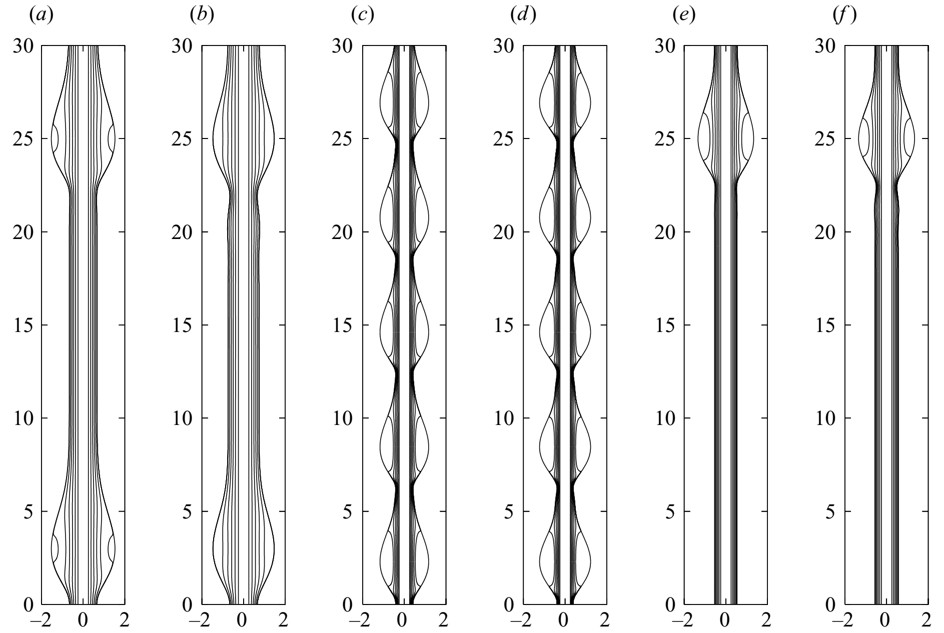

FIGURE 8. Profiles and streamlines in the moving frame of the TW solutions of model (4.16) (*a*, *c*, *e*) and of the CM equation (4.22) (*b*, *d*, *f*). (*a*, *b*), (*c*,*d*) and (*e*, *f*) correspond to the regimes a, b and c reported by Kliakhandler *et al.* (2001). Distances are given in dimensional units (mm).

The wavelength λ has been adjusted to its experimental value. Model (4.16) and CM equation (4.22) give comparable results, in good agreement with the experimental observations. Wave profiles and streamlines in the moving frame of reference are shown in figure 8. Dimensions have been chosen to enable a direct comparison with the experimental snapshots (Kliakhandler *et al.* 2001, figure 1). The agreement between both models is again very good. The sole noticeable difference is the presence of capillary ripples in front of the beads observed with the CM equation. Capillary ripples are almost absent from the solutions of model (4.16), in agreement with experimental observations. We note that the streamlines in the moving frame reveal large recirculation zones inside the beads in regime b and c. As in the moving frame the fluid moves upwards underneath the waves, the presence of recirculation zones proves that the beads carry mass. In fact, in regime b, the beads carry nearly all the fluid and the waves resemble drops sliding on a liquid substrate.

7. Time-dependent computations and wave selection

We now examine the spatio-temporal dynamics of a flow down a fibre. For this purpose we employed a second-order finite-differencing quasi-linearized Crank–Nicolson scheme. We impose simple soft boundary conditions at the outlet: the integral momentum balance (4.16*b*) is replaced at the last two nodes of the discretized domain with a simple linear hyperbolic (wave) equation $\partial_t q + v_{\mathrm{f}} \partial_x q = 0$ where v_f is set to unity in most simulations. A similar methodology is followed for the Trifonov and RL models. In the case of the CM equation, the high-order spatial derivatives were set equal to zero at the last two nodes while the parameter β was artificially set to zero in a 'damping layer' of typically 100 nodes. This simple procedure turns out to be sufficient and without any spurious backwards reflections of the waves. Following Chang, Demekhin & Kalaidin (1996), we have chosen a random-phase formulation of the noise applied at the inlet. The Fourier spectrum of the zero-mean perturbation $F(t)$ of the inlet flow rate contain frequencies of equal Fourier coefficients but with different phases obtained through a random-number generator. The coefficients of frequencies higher than a few times the linear critical frequency are set to zero to avoid instabilities of our numerical scheme.

We first present time-dependent simulations for the three regimes reported by Kliakhandler *et al.* (see table 1). All of them correspond to linearly absolutely unstable flows (indicated by crosses in figure 5*a*). The initial condition – a small hydraulic jump connecting two regions of different uniform thicknesses – therefore gives way to a regular wavetrain invading the whole computational domain. Snapshots of the film thickness at the end of the simulations for regimes a and b are displayed in figures 9 and 10. In regime a, model (4.16) shows that the regular global mode is disorganized downstream by a secondary instability. Intermittent coalescence events (one such event can be seen occurring at $x \approx 210$ mm) widen the spacing between the waves: the waves become more and more localized. At the final stage, we observe a train of solitary-like coherent structures (that resemble the infinite-domain solitary pulses computed in the previous section). These pulses are separated by portions of flat films of small but irregular thicknesses. The amplitudes and distances between the solitary pulses are in reasonable agreement with the experimental observations ($h_{max}^{expt} = 1.47$ mm and approximately 30 mm between pulses). In regime b, a stable regular global mode invades the entire computational domain. The wave characteristics compare well to the experimental observations (wavelength $\lambda = 5.84$ mm, speed $c = 7.2$ mm s^{-1}, maximum and minimum heights 0.90 mm and 0.17 mm) and correspond to a frequency, 1.23 Hz, close to the linear absolute frequency, 1.34 Hz. However, we have been unable to reproduce the irregular regime c reported in the experiments by Kliakhandler *et al.* (2001). In our simulations, a stable global mode (not shown) is again observed in the entire domain.

Time-dependent computations of the CM equation (4.22) show a radically different dynamics. In regime a, a slowly modulated wavetrain rapidly invades the entire computational domain whereas intermittent coalescence events are not observed. The average separation between neighbouring pulses, around 10 mm, is three times smaller than reported in experiments. The waves tend to group themselves in 'bound states' of two or three pulses as observed by Craster & Matar (2006).

In regime b, the global mode that sets in has a frequency 0.9 Hz which is approximately half the linear absolute frequency, 1.81 Hz. The wave length, ≈14 mm, is therefore approximately twice the experimental one, 6.2 mm. This selection of wave patterns different to that observed in the experiments might explain why Craster & Matar were unable to find TW solutions corresponding to the experimental wavelength for regime b. A growing modulation of the wave amplitude can be observed in figure 9(*b*) leading eventually to a disorganization of the wave pattern. As noted by Craster & Matar, it turns out that the periodic wavetrain solutions to the CM equation are unstable in regime b. In regime c (not shown) the resulting wave patterns are similar to those in regime b but more irregular.

Let us now present some time-dependent computations for the experimental conditions reported in the recent study by Duprat *et al.* (2007). Figure 11 shows the corresponding spatio-temporal diagrams. Duprat *et al.* used a fluid less viscous than Kliakhandler *et al.* (2001) and Craster & Matar (2006) so that inertia plays

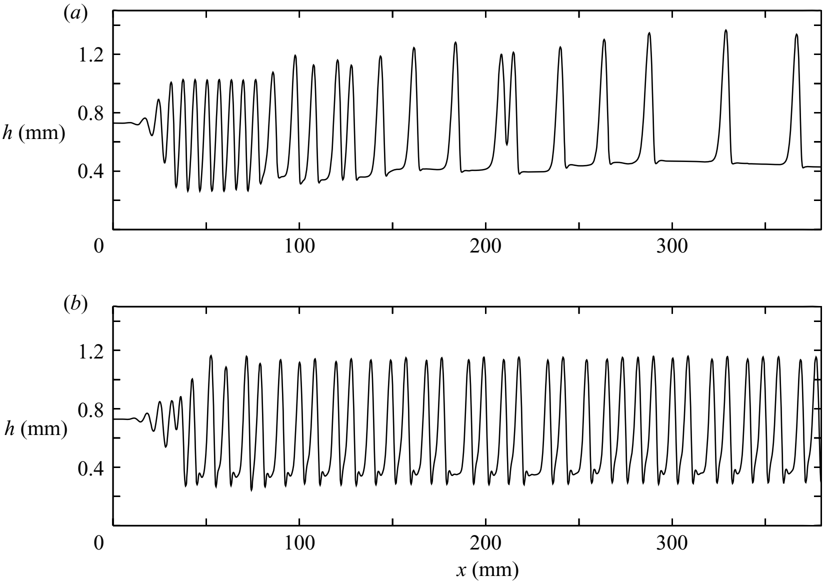

FIGURE 9. Computed film thickness as a function of the distance from the inlet. Parameters correspond to regime a in table 1. (*a*) Solution of model (4.16). (*b*) Solution of CM equation (4.22).

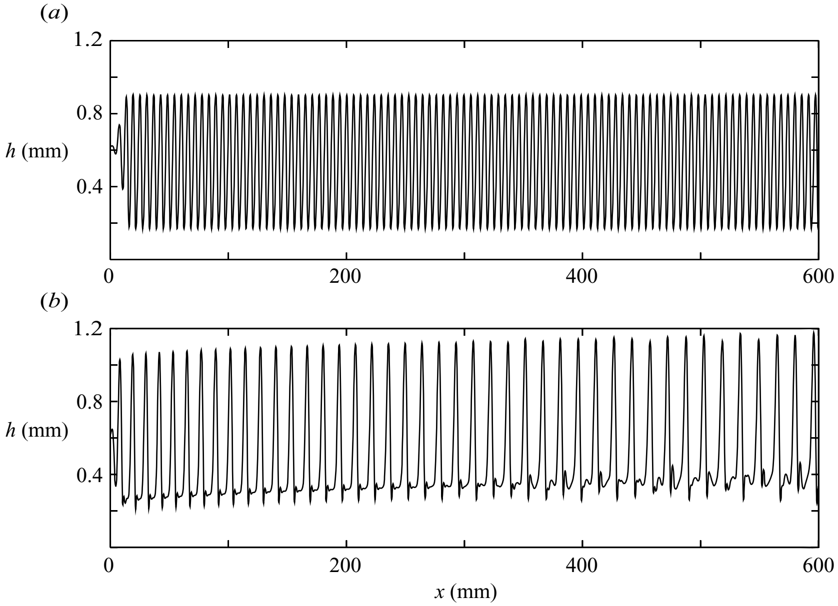

FIGURE 10. Computed film thickness as function of the distance from the inlet. Parameters correspond to regime b in table 1. (*a*) Solution of model (4.16). (*b*) Solution of CM equation (4.22).

a non-negligible role. We therefore compare simulations of model (4.16) and the Trifonov model.

The spatio-temporal diagrams depicted in figure 11 correspond to the 'permanent' wave regimes obtained at the end of the simulations to be contrasted with the

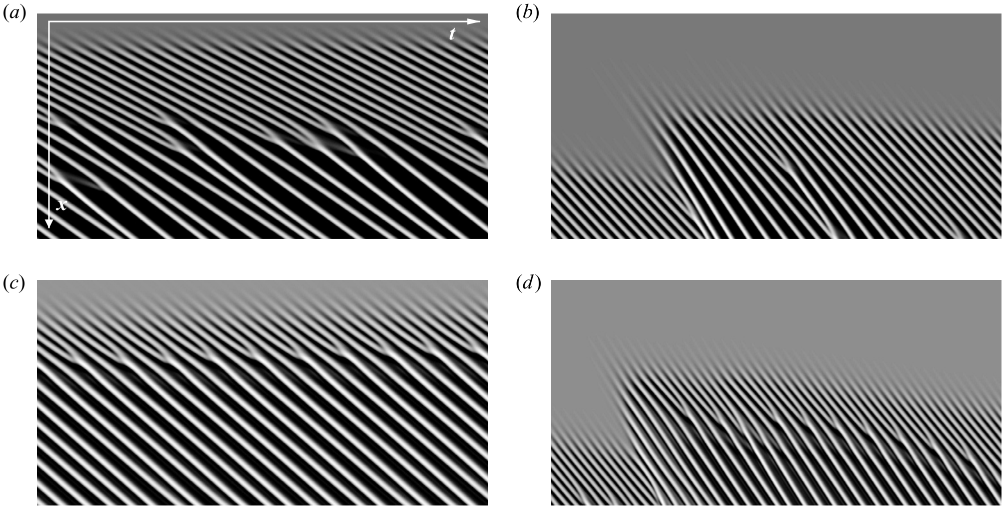

FIGURE 11. Spatio-temporal diagrams showing the response of the film to a coloured noise (see text). (*a*, *b*) Solutions of the second-order model (4.16). (*c*, *d*) Solutions to the Trifonov model. Parameters correspond to the experimental conditions (Duprat *et al.* 2007, figure 2, silicon oil v50 and $R = 0.32$ mm): (*a*–*c*) $q_N = 24$ mgs^{-1} ($\delta = 0.3$, $\tilde{\alpha} = 1.32$, $\eta = 0.19$), (*b*–*d*) $q_N = 77$ mgs^{-1} ($\delta = 1.3$, $\tilde{\alpha} = 1.80$, $\eta = 0.28$). Dark (light) regions correspond to small (large) elevations. Vertical and horizontal ranges are 4 s and 10 cm, respectively.

spatio-temporal diagrams reported in Duprat *et al.* An absolutely unstable flow (figures 11*a* and 11*c*) and a convectively unstable one (figures 11*b* and 11*d*) are shown. A small-amplitude coloured noise been has again been applied at the inlet, therefore sustaining the structures observed in the convectively unstable regime.

For the absolutely unstable flow, model (4.16) gives results in reasonable agreement with experimental observations (cf. figure 11*a*). A very regular wavetrain develops from the inlet but it is quickly destroyed. As in the experiment, this disorganization process looks irregular and is probably promoted by a secondary sideband instability. Waves of larger amplitudes and travelling at greater speeds emerge through intermittent coalescence events in a fashion that is comparable to the noise-driven transitions observed in the case of film falling down a planar vertical wall (Chang, Demekhin & Saprikin 2002). The simulation of the Trifonov model shows a different scenario. The wavetrain that emerges from the primary instability undergoes a subharmonic instability that doubles its frequency (cf. figure 11*c*). No further bifurcations are observable downstream.

The differences between the two spatio-temporal evolutions illustrated in figures 11(*a*) and 11(*c*) may be better understood by looking at the snapshots of the film thickness at the end of the simulations (cf. figure 12). In the case of model (4.16), solitary-like coherent structures emerging from the secondary instability of the primary regular wavetrain are again separated by portions of nearly flat films. The capillary oscillations/ripples preceding the solitary humps are small. In contrast, the snapshot of the film at the end of the simulation for the Trifonov model is quite different. The waves are not localized and the main humps are separated by secondary ones resembling the capillary oscillations/ripples preceding the γ_2 solitary waves. This observation suggests that the selection of either a subharmonic or a sideband secondary instability is responsible for the localisation of the waves, which in turn is strongly dependent on the streamwise viscous terms.

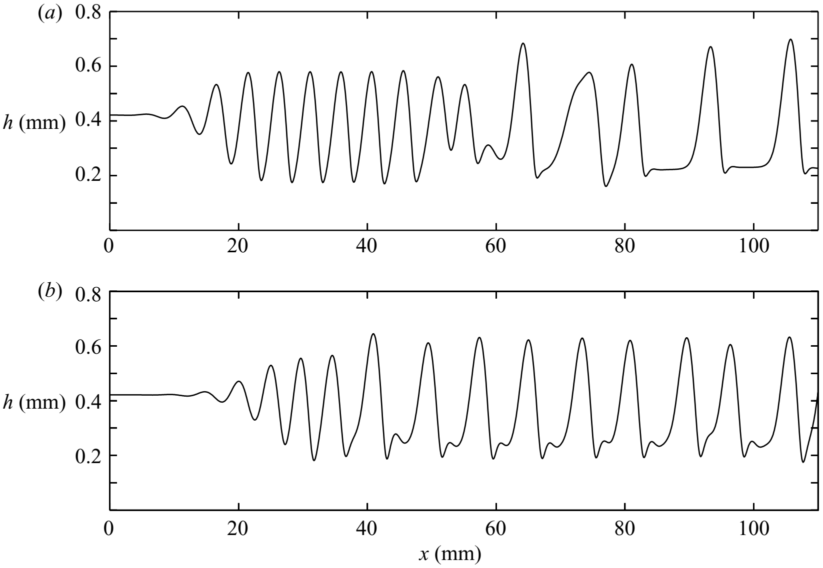

FIGURE 12. Film thickness as function of the distance from the inlet at the end of the simulations presented in figures 11(*a*) and 11(*c*); (*a*) Solution of model (4.16). (*b*) Solution of Trifonov model.

For the convectively unstable flow, the irregular motion of the 'healing length', i.e. the distance from the inlet at which the waves are first noticeable, resembles the experimental observations. The time-dependent computations of model (4.16) show some coalescence events as observed in the experimental spatio-temporal diagram (cf. figure 11*b*). It is, however, difficult to conclude that this is always the case since the number of coalescence events strongly depends on the amplitude and spectrum of the inlet experimental perturbation which is unknown. Simulations with the Trifonov model show again a tendency to period doubling not observed in the experiments but also a series of coalescence events are observed as in the experiment (cf. figure 11*d*). We note that in general the Trifonov model gives a larger number of coalescence events compared to (4.16) owing to the larger band of unstable wavenumbers, a consequence of neglecting streamwise viscous dissipation, which in turn leads to a larger susceptibility to noise.

Finally, we note that we have attempted to simplify our second-order model (4.16) by using polynomial expansions of the coefficients in the form of (4.13). Non-physical blow-ups in time-dependent computations were generally observed even at quite low values of the aspect ratio $\tilde{\alpha}$. This drawback is probably a manifestation of the poor convergence properties of the coefficients of our model due to the presence of the logarithmic function $\log(\tilde{\alpha})$ in these coefficients. This poor convergence is illustrated in figure 13(*a*) where we display the speed of linear kinematic and dynamic waves in the limit of negligible viscous dispersion ($\eta \to 0$) and large Reynolds numbers ($\beta/\delta \to 0$) corresponding to the $O(\tilde{\alpha}^2)$ expansion (4.13). For aspect ratios $\tilde{\alpha}$ above 1.2, the speed c_k of the kinematic waves lies in the interval $[c_{d-}, c_{d+}]$ which implies linear stability, in contradiction with the results from model (4.16) (compare figure 13(*a*) to figure 2(*a*)).

A similar drawback is observed with the RL model (see figure 13*b*). The spatial dynamics of the film predicted by this model is shown in figure 14 for the flow

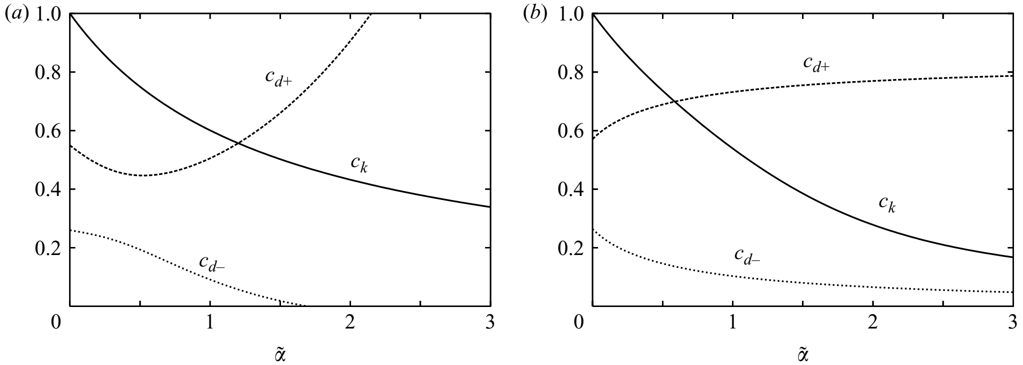

FIGURE 13. Speeds c_k (5.2) of kinematic waves and $c_{d\pm}$ (5.10) of dynamic waves as functions of the aspect ratio $\tilde{\alpha} = h_N/R$ in the limit of negligible viscous dispersion ($\eta \rightarrow 0$) and large Reynolds numbers ($\beta/\delta \rightarrow 0$). (*a*) Expansion (4.13); (*b*) RL model (4.14).

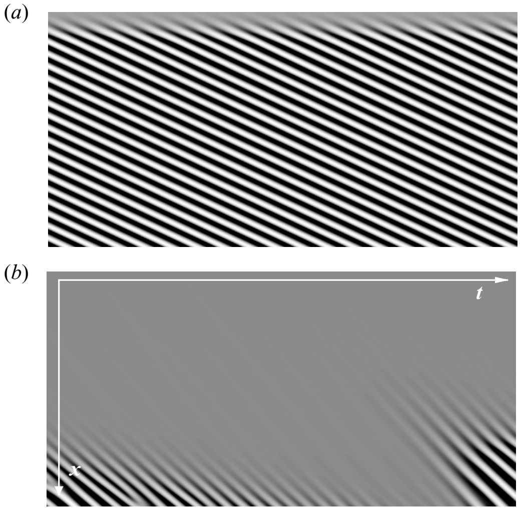

FIGURE 14. Spatio-temporal diagrams showing the response of the film to a coloured noise simulated with RL model (4.14). Parameters are $\delta = 0.3$, $\tilde{\alpha} = 1.32$ and $\eta = 0.19$ (*a*), and $\delta = 1.3$, $\tilde{\alpha} = 1.80$ and $\eta = 0.28$ (*b*). Vertical and horizontal ranges are 4 s and 10 cm, respectively. See also the caption of figure 11.

conditions corresponding to the experiments by Duprat *et al.* (2007). For the two simulations shown in the figure, the aspect ratio $\tilde{\alpha}$ is $O(1)$ as in the experiments and the RL model unphysically stabilises the hydrodynamic K mode (the RL model always suppresses the K mode for $\tilde{\alpha} \gtrsim 0.6$). As a consequence, the base flow is less unstable, and for similar inlet noise, the spatial development of the waves is delayed in the convective case (compare figures 14*b* and 11*b*). In the absolute case, a very regular wavetrain is observed in disagreement with the experimental observations.

8. Summary and conclusions

We have formulated, within the framework of the boundary-layer approximation, a low-dimensional model that consists of two coupled evolution equations for the film thickness h and the flow rate q. The model is rather general: it accounts for both inertial and streamwise viscous effects, it is not limited to small aspect ratios h/R and is applicable even if $\Gamma = O(1)$. Previous one-equation models are recovered in the appropriate limit. The key steps of our approach are: (i) elimination of the pressure by integrating the cross-stream momentum balance; (ii) projection of the velocity field onto an appropriately chosen set of test functions assuming small departures from the Nusselt uniform film velocity distribution. As in the planar case (Ruyer-Quil & Manneville 2002), we have shown that the use of the Galerkin weighted residual method is the optimum one leading to the desired formulation with a minimum of algebra.

In the linear regime, an excellent agreement with the Orr–Sommerfeld analysis of the primitive equations is attained. Streamwise viscous diffusion was shown to have a dispersive effect. The role of the K instability has been understood within the Whitham wave hierarchy framework (Whitham 1974). Streamwise viscous diffusion was shown to play a stabilising role by decreasing the speed of the kinematic waves.

In the nonlinear regime, TW branches of solutions have been obtained by continuation and have been favourably compared to the experiments by Kliakhandler *et al.* (2001). Time-dependent computations show that our second-order model recovers the regimes observed experimentally by Kliakhandler *et al.*, except for the irregular motion of large waves at very small flow rate (‘regime c’). Good agreement has also been obtained with the recent experiments by Duprat *et al.* (2007) for which the wave dynamics in the absolute and convective regimes are recovered. In contrast, by neglecting streamwise viscous diffusion, the CM evolution equation (4.22) overestimates the speed of linear waves. Our simulations of the spatial evolution of the flow then reveal that the wave selection observed with the CM equation does not correspond to the experimental observations. Therefore, the CM equation should be used with caution and certainly not to describe the spatio-temporal dynamics. The Trifonov model suffers from similar limitations. In the linear regime, it overestimates the range of unstable wavenumbers. Time-dependent computations in the nonlinear regime reveal a subharmonic secondary instability that was not observed in the experiments by Duprat *et al.*

In conclusion, despite its apparent ‘complexity’, the model in equation (4.16) performs well in both linear and nonlinear regimes and captures the dynamics for the largest possible range of parameters.

C.R.-Q. would like to thank S. Ndoumbe and F. Lusseyran with whom a preliminary study was undertaken, and Y. Bardoux for a careful reading of the manuscript. We acknowledge financial support through a travel grant supported by the Franco-British Alliance Research Partnership Programme. S.K. thanks Laboratoire FAST for hospitality.

Appendix A. Boundary-layer approximation for $\Gamma = O(1)$

Here we consider the more involved case (ii) with $\Gamma = O(1)$ and $\epsilon^{3/2} \ll h_{\mathrm{N}} \ll 1$. In the first instance we neglect terms $O(\epsilon^3 h_{\mathrm{N}})$ and higher associated with the viscous part of the pressure in the normal stress balance (2.1*e*) and approximate the pressure as,

$$p|_h = \{\text{right-hand-side of (3.5)}\} + O\left((\partial_x h)^2 \partial_{xx} h,\ \frac{\epsilon^4}{R+h}\right), \tag{A 1}$$

where the neglected terms are of $O(\epsilon^4/h_{\mathrm{N}}, \epsilon^4\alpha)$. As a result $p|_h$ is identical to that in (3.5). The tangential-stress boundary condition (2.1*f*) up to of $O(\epsilon^2 h_{\mathrm{N}})$ yields equation (3.6). Hence the contribution of the term $\partial_x h \partial_r u_x$ in (A 1) is of $O(\epsilon^3 h_{\mathrm{N}})$ and must be neglected. As a result p is identical to that in (3.7) but now terms of $O(\epsilon^4/h_{\mathrm{N}}, \epsilon^4\alpha, \epsilon^3 h_{\mathrm{N}}, \epsilon^2 h_{\mathrm{N}}^4)$ are neglected which is indeed the case provided that $\max\{\epsilon^3/h_{\mathrm{N}}, \epsilon h_{\mathrm{N}}, h_{\mathrm{N}}^4, \epsilon^5/h_{\mathrm{N}}^3, \epsilon^{9/4}\} \ll \alpha \ll \min\{1/(\epsilon^2 h_{\mathrm{N}}), h_{\mathrm{N}}/\epsilon^3, h_{\mathrm{N}}^{3/2}/\epsilon^2, 1/\epsilon^{3/2}, h_{\mathrm{N}}/\epsilon^5\}$ and $\epsilon^{4/5} \ll h_{\mathrm{N}} \ll 1$ (once again through a detailed examination of the orders of magnitude of the retained over the neglected terms). As an example, with $h_{\mathrm{N}} \sim \epsilon^{1/2}$, $\epsilon^{3/2} \ll \alpha \ll \epsilon^{-5/4}$ and α is allowed to take both small and large values, for example $\alpha \sim \epsilon^{\pm 1/2}$ which also satisfies the requirement αh_{N} at most of $O(1)$. K_{az} is also identical to (3.8) but now terms of $O(\epsilon^4\alpha)$ and higher are neglected (moreover, $\alpha h \rightarrow 0$ now does not imply the planar limit as in case (i)). Hence the final streamwise momentum equation for case (ii) is identical to (3.9) for case (i).

Finally, we note that the order-of-magnitude assignment $h_{\mathrm{N}} \sim 1$ in case (i) can be relaxed, allowing α and h_{N} to be both small and large (and so that the requirement αh_{N} at most of $O(1)$ is still satisfied). For this purpose we would have to repeat the analysis for case (ii) to obtain lower/upper bounds on h_{N} and α but now with $\Gamma = O(\epsilon^{-2})$ instead of $\Gamma = O(1)$.

Appendix B. Coefficients of models (4.10) and (4.12)

The coefficients of the first-order momentum balance (4.10) consist of ratios of polynomials in b and $\log(b)$ where $b = 1 + \alpha h$:

$$\phi = \{3[(4\log(b) - 3)b^4 + 4b^2 - 1]\}/[16(b-1)^3], \tag{B 1a}$$

$$F = 3F_a/[16(b-1)^2 \phi F_b], \tag{B 1b}$$

$$\begin{aligned} F_a = {} & -301b^8 + 622b^6 - 441b^4 + 4\log(b)\{197b^6 - 234b^4 + 6\log(b) \\ & \times[16\log(b)b^4 - 36b^4 + 22b^2 + 3]b^2 + 78b^2 + 4\}b^2 + 130b^2 - 10, \end{aligned} \tag{B 1c}$$

$$F_b = 17b^6 + 12\log(b)[2\log(b)b^2 - 3b^2 + 2]b^4 - 30b^4 + 15b^2 - 2, \tag{B 1d}$$

$$G = G_a/[64(b-1)^4 \phi^2 F_b], \tag{B 1e}$$

$$\begin{aligned} G_a = {} & 9b\{4\log(b)[-220b^8 + 456b^6 - 303b^4 + 6\log(b)(61b^6 - 69b^4 \\ & + 4\log(b)(4\log(b)b^4 - 12b^4 + 7b^2 + 2)b^2 + 9b^2 + 9)b^2 + 58b^2 + 9]b^2 \\ & + (b^2-1)^2(153b^6 - 145b^4 + 53b^2 - 1)\}, \end{aligned} \tag{B 1f}$$

$$I = 64(b-1)^5 \phi^2/[3F_b]\,. \tag{B 1g}$$

Expressions (B 1) can be contrasted to the corresponding ones for the first-order averaged momentum balance obtained by Trifonov (1992) with a uniform weight:

$$F = \frac{6 - 45b^2 + 90b^4 - 51b^6 - 36b^4\log(b)[2 - 3b^2 + 2b^2\log(b)]}{32(b-1)^5\phi}, \tag{B 2a}$$

$$G = G_a/\{512(b-1)^7\phi^3\}, \tag{B 2b}$$

$$\begin{aligned} G_a = {} & 9b\{(b^2-1)^2(1 - 26b^2 + 37b^4) - 8b^2\log(b)[2 + 12b^2 - 36b^4 + 22b^6 \\ & + 3b^2\log(b)(3 + 4b^2 - 9b^4 + 4b^4\log(b))]\}, \end{aligned} \tag{B 2c}$$

$$I = (b+1)/2\,. \tag{B 2d}$$

The coefficients of the second-order corrections in (4.12) are:

$$J = J_a/[128(b-1)^4\phi^2 F_b], \tag{B 3a}$$

$$\begin{aligned} J_a = 9\{&(490b^8 - 205b^6 - 235b^4 + 73b^2 - 3)(b^2 - 1)^3 \\ &+4b^2 \log(b)[2b^4 \log(b)(72 \log(b)(2 \log(b)b^4 - 6b^4 + b^2 + 6)b^4 \\ &+(b - 1)(b + 1)(533b^6 - 109b^4 - 451b^2 + 15)) \\ &-3(b^2 - 1)^2(187b^8 - 43b^6 - 134b^4 + 17b^2 + 1)]\}, \end{aligned} \tag{B 3b}$$

$$K = 3K_a/[16b^3(b - 1)^2\phi F_b], \tag{B 3c}$$

$$\begin{aligned} K_a = {}&4b^4 \log(b)(233b^8 - 360b^6 + 12 \log(b)(12 \log(b)b^4 - 25b^4 + 12b^2 + 9)b^4 \\ &+54b^4 + 88b^2 - 15) - (b^2 - 1)^2(211b^8 - 134b^6 - 56b^4 + 30b^2 - 3), \end{aligned} \tag{B 3d}$$

$$L = L_a/[8b(b - 1)^2\phi F_b], \tag{B 3e}$$

$$\begin{aligned} L_a = {}&4b^2 \log(b)\{6 \log(b)(12 \log(b)b^4 - 23b^4 + 18b^2 + 3)b^4 + (b - 1)(b + 1) \\ &\times(95b^6 - 79b^4 - 7b^2 + 3)\} - (b^2 - 1)^2(82b^6 - 77b^4 + 4b^2 + 3), \end{aligned} \tag{B 3f}$$

$$M = 3 + [24 \log(b)b^8 - 25b^8 + 48b^6 - 36b^4 + 16b^2 - 3]/[2b^2 F_b]. \tag{B 3g}$$

REFERENCES

Alekseenko, S. V., Nakoryakov, V. Y. & Pokusaev, B. G. 1985 Wave formation on a vertical falling liquid film. *AIChE J.* **31**, 1446–1460.

Brevdo, L., Dias, F., Bridges, T. J. & Laure, P. 1999 Convective unstable wave packets in a film flow down an inclined plane. *J. Fluid Mech.* **396**, 37–71.

Chang, H.-C., Demekhin, E. A. & Kalaidin, E. 1996 Simulation of noise-driven wave dynamics on a falling film. *AIChE J.* **42**, 1553–1568.

Chang, H.-C., Demekhin, E. A. & Saprikin, S. 2002 Noise-driven wave transitions on a vertically falling film. *J. Fluid Mech.* **462**, 255–283.

Craster, R. V. & Matar, O. K. 2006 On viscous beads flowing down a vertical fibre. *J. Fluid Mech.* **553**, 85–105.

Doedel, E. J., Champneys, A. R., Fairgrieve, T. F., Kuznetsov, Y. A., Sandstede, B. & Wang, X.-J. 1997 Auto97: Continuation and bifurcation software for ordinary differential equations. *Tech. Rep.* Department of Computer Science, Concordia University, Montreal, Canada (available by FTP from ftp.cs.concordia.ca in directory pub/doedel/auto).

Duprat, C., Ruyer-Quil, C., Kalliadasis, S. & Giorgiutti-Dauphiné, F. 2007 Absolute and convective instabilities of a film flowing down a vertical fiber. *Phys. Rev. Lett.* **98**, 244502.

Frenkel, A. L. 1992 Nonlinear theory of strongly undulating thin films flowing down vertical cylinders. *Europhys. Lett.* **18**, 583–588.

Gaster, M. 1962 A note on the relation between temporally-increasing and spatially increasing disturbances in hydrodynamic stability. *J. Fluid Mech.* **14**, 222–224.

Huerre, P. & Rossi, M. 1998 Hydrodynamic instabilities in open flows. In *Hydrodynamic and Nonlinear Instabilities* (ed. C. Godréche & P. Manneville), pp. 81–294. Cambridge University Press.

Kalliadasis, S. & Chang, H.-C. 1994 Drop formation during coating of vertical fibres. *J. Fluid Mech.* **261**, 135–168.

Kliakhandler, I. L., Davis, S. H. & Bankoff, S. G. 2001 Viscous beads on vertical fibre. *J. Fluid Mech.* **429**, 381–390.

Ooshida, T. 1999 Surface equation of falling film flows with moderate Reynolds number and large but finite Weber number. *Phys. Fluids* **11**, 3247–3269.

Quéré, D. 1990 Thin films flowing on vertical fibers. *Europhys. Lett.* **13**, 721–726.

Quéré, D. 1999 Fluid coating on a fiber. *Annu. Rev. Fluid Mech.* **31**, 347–384.

Rayleigh, Lord 1878 On the stability of liquid jets. *Proc. Lond. Math. Soc.* **10**, 4.

Roberts, A. J. & Li, Z. 2006 An accurate and comprehensive model of thin fluid flows with inertia on curved substrates. *J. Fluid Mech.* **553**, 33–73.

Roy, R. V., Roberts, A. J. & Simpson, A. J. 2002 A lubrication model of coating flows over a curved substrate in space. *J. Fluid Mech.* **454**, 235–261.

Ruyer-Quil, C. & Manneville, P. 2000 Improved modeling of flows down inclined planes. *Eur. Phys. J.* B **15**, 357–369.

Ruyer-Quil, C. & Manneville, P. 2002 Further accuracy and convergence results on the modeling of flows down inclined planes by weighted-residual approximations. *Phys. Fluids* **14**, 170–183.

Scheid, B., Ruyer-Quil, C. & Manneville, P. 2006 Wave patterns in film flows: modelling and three-dimensional waves. *J. Fluid Mech.* **562**, 183–222.

Shkadov, V. Ya. 1967 Wave flow regimes of a thin layer of viscous fluid subject to gravity. *Izv. Akad. Nauk SSSR, Mekh. Zhidk Gaza* **1**, 43–51 (English translation in *Fluid Dyn.* **2**, 29–34, 1970, Faraday Press, NY).

Shkadov, V. Ya. 1977 Solitary waves in a layer of viscous liquid. *Izv. Ak. Nauk SSSR, Mekh. Zhid Gaza* **1**, 63–66.

Sisoev, G. M., Craster, R. V., Matar, O. K. & Gerasimov, S. V. 2006 Film flow down a fibre at moderate flow rates. *Chem. Eng. Sci.* **61**, 7279–7298.

Smith, M. K. 1990 The mechanism for the long-wave instability in thin liquid films. *J. Fluid Mech.* **217**, 469–485.

Trifonov, Yu. Ya 1992 Steady-state travelling waves on the surface of a viscous liquid film falling down vertucal wires and tubes. *AIChE J.* **38**, 821–834.

Whitham, G. B. 1974 *Linear and Nonlinear Waves*. Wiley-Interscience.